UNIVERSITAT DE BARCELONA

Avenços en l'adquisició i interpretació de dades geoelèctriques

Fabián Bellmunt Traver

Grup d'Exploració Electromagnètica i Sísmica
Institut de Recerca Geomodels
Departament de Geodinàmica i Geofísica
Facultat de Geologia. Universitat de Barcelona

Avenços en l'adquisició i interpretació de dades geoelèctriques

Memòria presentada per Fabián Bellmunt Traver per a optar al títol de Doctor dins del programa de doctorat de Ciències de la Terra de la Universitat de Barcelona. Aquesta memòria ha estat realitzada baix la direcció del Dr. Alejandro Marcuello Pascual (Universitat de Barcelona).

Fabián Bellmunt Traver
Barcelona, Setembre 2015

Dr. Alejandro Marcuello Pascual
Director y tutor de la tesi

Annex

A continuació s'adjunten les tres publicacions originals que conformen aquesta tesi i que s'han introduït a la presentació:

Publicació 1

Bellmunt, F., Marcuello, A, (2011). **Method to obtain standard pseudosections from pseudo pole-dipole arrays.** Journal of Applied Geophysics, 75, 419-430.

Journal of Applied Geophysics 75 (2011) 419–430

Contents lists available at SciVerse ScienceDirect

Journal of Applied Geophysics

journal homepage: www.elsevier.com/locate/jappgeo

Method to obtain standard pseudosections from pseudo pole–dipole arrays

Fabián Bellmunt *, Alex Marcuello

Geodynamics and Basin research Group, Dept. of Geodynamics and Geophysics, BKC, University of Barcelona, Martí Franquès, s/n, 08028 - Barcelona, Spain

ARTICLE INFO

Article history:
Received 6 November 2010
Accepted 26 July 2011
Available online 27 August 2011

Keywords:
Electrical resistivity tomography
Multichannel acquisition
Resistivity
Dataset optimization
Pseudo pole–dipole array

ABSTRACT

This study deals with electrical resistivity tomography data and it is addressed at obtaining, from linear combinations of data, other datasets not directly measured. The method presented here allows performing the fieldwork systematically, without deciding the type of the more suitable common electrode array (e.g. Wenner, Wenner-Schlumberger, dipole–dipole or multiple-gradient) until or even after the interpretation time. The electrode configuration used by this method is denoted as pseudo pole–dipole array, because it is based on the standard pole–dipole one, but avoiding the disadvantage of locating the remote electrode far away from the profile (to "infinity"). The pseudo pole–dipole datasets can be acquired with common equipment using standard pole–dipole recording sequences. Once the desired datasets have been calculated, they can be inverted using standard interpretation software. The procedure used allows a data quality control to be introduced that is similar to the one based on normal and reciprocal measurements. To assess the method we considered noise-contaminated model responses as well as field data. It has been applied to build dipole–dipole and Wenner-Schlumberger datasets. Results show the suitability of both, the proposed method and the quality control.

1. Introduction

When conducting resistivity investigations (in connection with geology, engineering or other fields), a common occurring dilemma in the electrical resistivity tomography (ERT) is the selection of the electrode configuration that would respond best to the geoelectrical structure. The choice is usually made by considering one's own experience and a reasonable acquisition time. The characteristics of each electrode array, in terms of depth of investigation, sensitivity to horizontal or vertical variations and signal strength are well known (e.g. Loke, 2001, 2004). Numerical forward modelling has become an efficient tool for these types of study, showing how markedly different anomaly signatures are obtained using different electrode configurations for the same model (Dahlin and Zhou, 2004). Sometimes a mixed array, where apparent resistivity pseudosection is built using different datasets, appears to offer a more detailed image of the subsurface (Athanasiou et al., 2007; Candansayar, 2008; Zhou et al., 2002). In areas with basic or no geological information, it would be desirable to acquire a profile with different electrode configurations, but this could present problems due to acquisition time constraints rather than technical considerations.

Xu and Noel (1993) stated that it is possible to obtain datasets for any electrode configuration from linear combination of a non-unique complete dataset. They affirmed that the pole–pole configuration provided the best choice for simple and straightforward transformations. However, Beard and Tripp (1995) stated that even modest levels of noise the transformations may be considerably distorted and significant information can be lost using the pole–pole array in this manner. For this reason, it is commonly used for numerical forward modelling.

Three-electrode configurations have also been presented as a choice to compute other datasets, e.g. dipole–dipole or Schlumberger datasets (Candansayar and Basokur, 2001; Coggon, 1973; Karous and Pernu, 1985). However, the two- and three-electrode configurations are limited by the electrode at infinity, which is not always possible (e.g. in urban areas or rugged terrains).

The method proposed here uses a four-electrode configuration and lies in the tri-potential method (Carpenter, 1955; Carpenter and Habberjam, 1956), whereby the relations between three Wenner resistances (alpha, beta and gamma) are derived.

Taking into account that the Wenner, the Wenner-Schlumberger, the dipole–dipole and recently the multiple-gradient (Dahlin and Zhou, 2006) configurations are commonly used, the method presented here was designed to obtain these datasets, which can be further inverted using standard interpretation software.

The estimation of ERT data errors is a key aspect for the assessment of the proposed method. Usually, two (complementary) perspectives can be considered: repeatability and normal and reciprocal measurements. The first one consists of acquiring repeated measurements at the same electrode position to obtain statistical parameters, like standard deviation, to give an estimate error. This process often underestimates the true noise level, even in datasets collected several days apart (LaBrecque et al., 1996), and data outliers may result from highly stable repeated

* Corresponding author.
E-mail addresses: fbellmunt@ub.edu (F. Bellmunt), alex.marcuello@ub.edu (A. Marcuello).

0926-9851/$ – see front matter © 2011 Elsevier B.V. All rights reserved.
doi:10.1016/j.jappgeo.2011.07.020

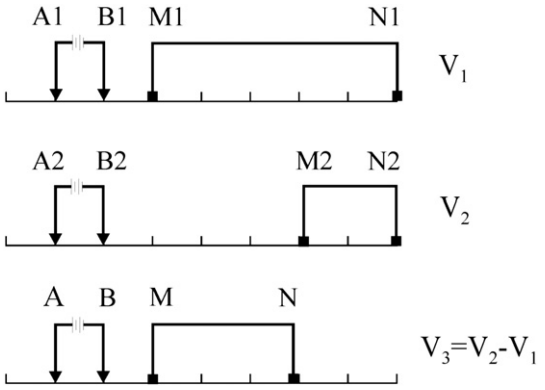

Fig. 1. Sketch of the additive property of the electric potential for a generic four-electrode configuration. A–B and M–N are the current and potential electrodes respectively, and V corresponds to the electric potential difference.

data (e.g. due to capacitive coupling effects). Therefore, a low standard deviation does not guarantee good quality data (Zhou and Dahlin, 2003). The second perspective, normal and reciprocal measurements, considers that receiver and transmitter are interchanged to obtain two independent measurements at the same point (Parasnis, 1988). The error is then taken as the difference between both measurements. This scheme can detect problems that may not be observed from repeatability checking, such as bad grounding of electrodes. Therefore, it will offer a better data quality control; however, it has the inconvenience of increasing the measuring time.

This paper aims to achieve two objectives: 1) to present a simple method to calculate datasets that are not directly measured (e.g. Wenner-Schlumberger and dipole–dipole) from a proposed configuration (pseudo pole–dipole array, pPD) and 2) to establish a data quality control, comparable to the normal and reciprocal measurements, without increasing the measuring time.

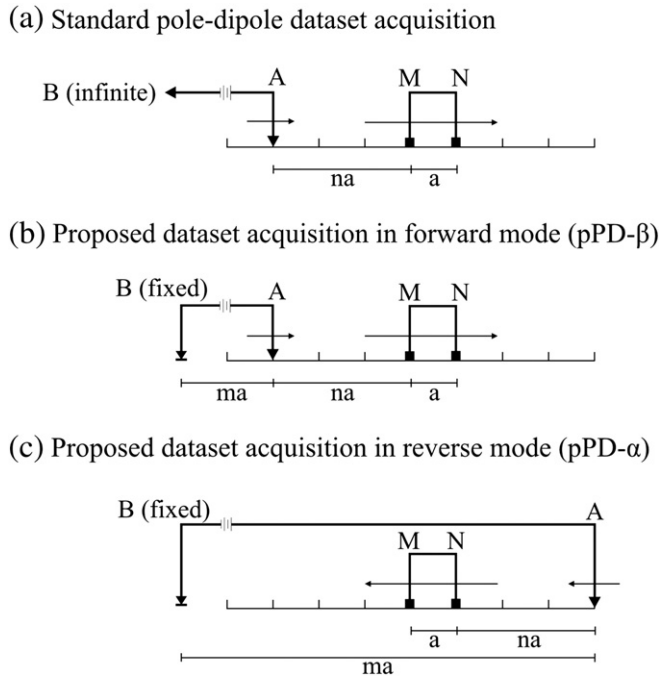

Fig. 2. Sketch of the electrode configurations to acquire the standard pole–dipole dataset (a), and the proposed dataset in forward (b) and reverse (c) modes. A–B and M–N are the current and potential electrodes respectively, "a" is the electrode spacing, "n" is the level of depth, and "m" is a A–B distance factor.

2. Procedure and pseudo pole–dipole (pPD) Array

To obtain datasets not directly measured from pseudo pole–dipole (pPD) array, relations between datasets have to be known. Relations between the measured and calculated datasets are based on the tri-potential method, on the reciprocity theorem (Carpenter, 1955; Habberjam, 1967; Parasnis, 1988; Van Nostrand and Cook, 1966), and on the additive properties of the electric potential (see Fig. 1), which has been normalized by the injected current. Because this normalized potential has units of electrical resistance, we prefer the notation of "transfer resistance". The apparent resistivity can be easily obtained by multiplying the transfer resistance and the geometrical factor K, which only depends on electrode location. If the geometric factor is assumed error-free, the relative error of both apparent resistivity and transfer resistance coincides.

The array proposed in this work is similar to the standard pole–dipole array, but locating the remote electrode (denoted B in this paper) in a closer position to the profile. As the standard pole–dipole array, it consists of two deployments, the forward (pPD-β) and the reverse (pPD-α) ones. A comparison between these deployments is shown in Fig. 2 (note that measured potentials are positive for pPD-β, but negative for pPD-α). They can be implemented easily in common instrumentation, since recording sequences are equivalent to the pole–dipole one, but locating the electrode B near profile.

Next, we present the transformations from pPD datasets to dipole–dipole and Wenner-Schlumberger ones.

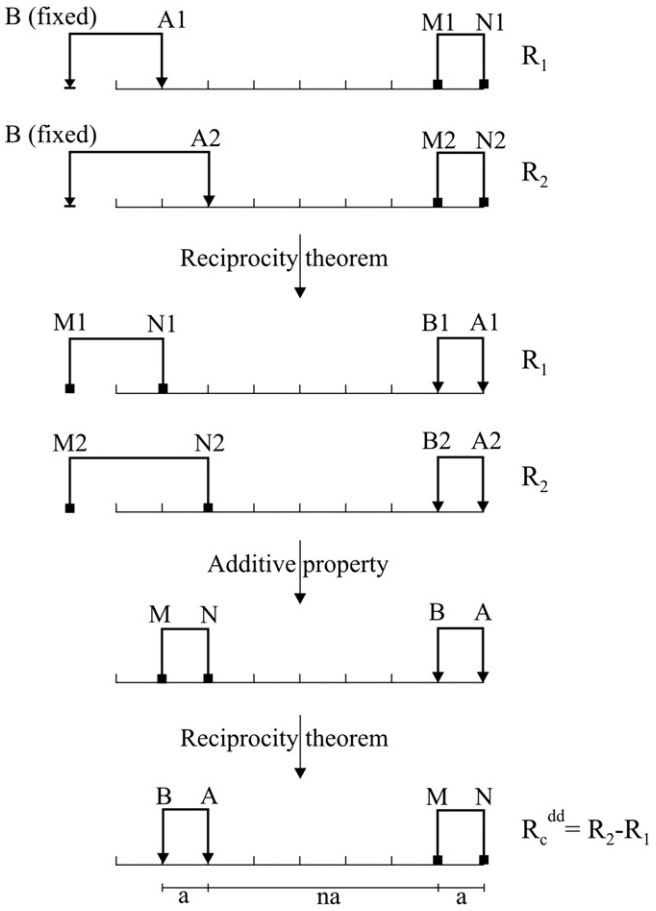

Fig. 3. Steps to obtain the dipole–dipole transfer resistances from the proposed dataset resistances. The reciprocity theorem and the additive property of electric potential are used. "a" is the electrode spacing and "n" is the level of depth.

2.1. Dipole–dipole dataset construction

Fig. 3 shows relations between the pPD transfer resistances and the dipole–dipole ones. Each dipole–dipole transfer resistance can be calculated independently from forward and reverse deployments (pPD-β and pPD-α). Note that the reciprocity theorem is applied.

$$R_2 - R_1 = R_c^{dd} \tag{1}$$

where R_1 and R_2 are the measured pPD transfer resistances (in forward or reverse mode), and R_c^{dd} is the calculated dipole–dipole transfer resistance.

The transfer resistances R_2 and R_1 correspond to levels n and $n+1$ respectively in the pPD pseudosection, and R_c^{dd} corresponds to level n in the dipole–dipole pseudosection. Therefore, $n+1$ levels are required in the pPD pseudosection to reproduce up to n levels in the dipole–dipole one.

2.2. Wenner-Schlumberger dataset construction

To build the Wenner-Schlumberger dataset, both pPD-α and pPD-β deployments are needed. Fig. 4 shows relations between the pPD-α and pPD-β transfer resistances and the Wenner-Schlumberger one. Notice that both deployments have the electrode B in the same position (see Fig. 2). Once the reciprocity theorem is applied, relationships between pPD-α, pPD-β and Wenner-Schlumberger datasets are much clearer.

$$R_\alpha - R_\beta = R_c^{WS} \tag{2}$$

Because R_α is negative and R_β is positive, R_c^{WS} is negative, therefore Eq. (2) can also be expressed as

$$|R_\alpha| + |R_\beta| = |R_c^{WS}| \tag{3}$$

where R_α and R_β are the pPD-α and pPD-β transfer resistance respectively, and R_c^{WS} is the calculated Wenner-Schlumberger one.

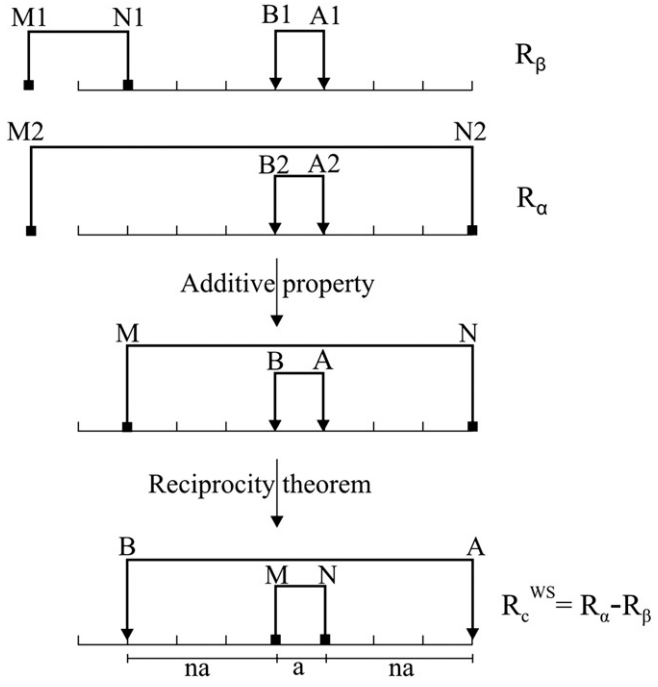

Fig. 4. Steps to obtain the Wenner-Schlumberger transfer resistances from the proposed dataset resistances. The reciprocity theorem and the additive property of electric potential are used. "a" is the electrode spacing and "n" is the level of depth.

Table 1
Number of injections for a 64-electrode dipole–dipole array as a function of the number of levels (N) and the number of channels (c).

N \ c	1	4	16	32	64
15	810	220	61	61	61
30	1395	376	106	61	61
45	1755	468	135	90	61
61	1891	496	148	90	61

Expressions relating pPD datasets with other common datasets (Wenner or multiple-gradient arrays) can be obtained by a similar procedure.

The proposed array presents two other features that need to be considered, and they are related to the acquisition time and the size of recorded signals. Both features are discussed below.

2.3. Acquisition time

Taking into account that pole–dipole and dipole–dipole datasets are comparable in number of data, the following expression can be assumed to estimate their measuring time, t:

$$t = i(sT + r) \tag{4}$$

where i is the number of current injections (in monochannel systems, this corresponds to the number of data), s is the average of cycles per measurement or stack, T is the time length cycle, and r is a constant, which accounts the time used to control and to record the data, and it is associated to the system hardware.

The multichannel system works on reducing the number of injections (i). This number of injections depends on the array type, the number of channels (c), electrodes (e) and levels in the pseudosection (N). The dipole–dipole array is one of the most efficient arrays with multichannel acquisition, and an expression for their number of injections (and by extension for the pPD array) is:

$$i = I_M\left\{(e-3) - \frac{1}{2}c(I_M - 1)\right\} \tag{5}$$

where I_M is the maximum number of injections required for a single current dipole. It is calculated from expression $I_M = int[(N-1)/c] + 1$, where $int(x)$ gives the integer part of x (see Appendix A for details).

As a representation of recording time, the number of injections needed to reach 15, 30, 45 and 61 levels, with a 64-electrode dipole–dipole array and instruments with 1, 4, 16, 32 and 64 channels, is shown in Table 1. There it can be seen that from a given number of data, there is no time reduction when increasing the number of channels.

Regarding the acquisition time, multichannel systems are highly suitable for dipole–dipole and pPD arrays, still suitable for Wenner-Schlumberger arrays (but less efficient than the dipole–dipole one), and not suitable for the Wenner array. Although the method requires

Table 2
Expressions of the inverse of the geometric factor (K^{-1}) for different electrode arrays.

Electrode array	Inverse of th geometric factor (K^{-1})
Wenner-Schlumberger	$\frac{-1}{\pi a}\left[\frac{1}{n(n+1)}\right]$
pole–dipole	$\frac{1}{2\pi a}\left[\frac{1}{n(n+1)}\right]$
dipole–dipole	$\frac{1}{\pi a}\left[\frac{1}{n(n+1)(n+2)}\right]$
pseudo pole–dipole, pPD-α	$\frac{-1}{2\pi a}\left[\frac{1}{n(n+1)} + \frac{1}{(m-n)(m-n-1)}\right]$
pseudo pole–dipole, pPD-β	$\frac{1}{2\pi a}\left[\frac{1}{n(n+1)} - \frac{1}{(m+n)(m+n+1)}\right]$

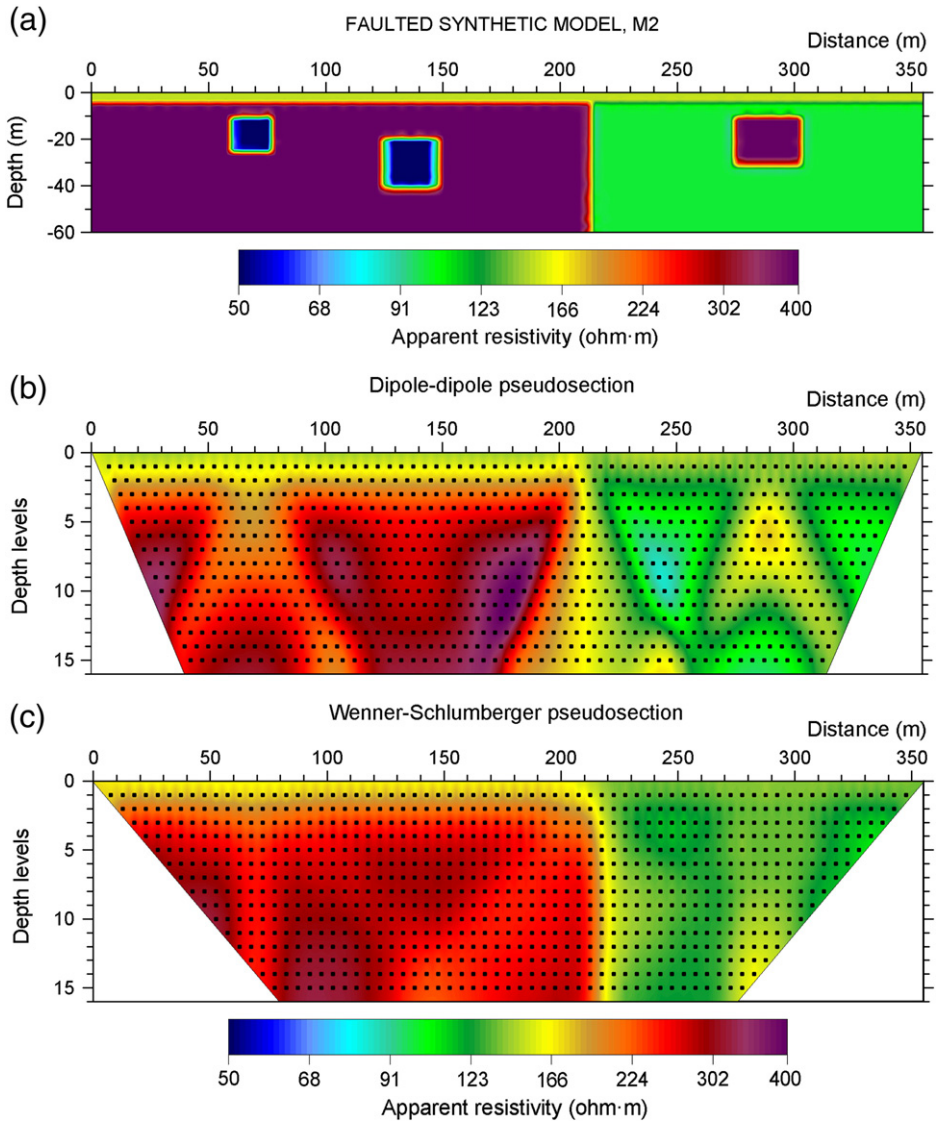

Fig. 5. Model M2 and error-free model responses. (a) Model M2, (b) dipole–dipole apparent resistivity pseudosection and (c) Wenner-Schlumberger apparent resistivity pseudosection.

both forward and reverse pPD deployments to be carried out, the acquisition time is not an important matter if such multichannel instruments are used.

2.4. Size of the recorded signal

The way to compare signals of different arrays is to use the geometric factor K, whose inverse (K^{-1}) describes a normalized potential distribution in a homogeneous halfspace. Table 2 summarises different expressions of K^{-1}. Note that the sign of the geometric factor is referred to the configurations presented in Figs. 2, 3 and 4. Their development shows that the signal size for the pPD deployments is lower than or equal to the Wenner-Schlumberger one, and higher than or equal to the dipole–dipole one. It can be noticed that proposed configurations combine characteristics, in terms of signal-size, of pole–dipole, dipole–dipole, gradient and Wenner-Schlumberger arrays.

In summary, it can be seen that pPD-β deployment behaves essentially like a dipole–dipole array when current electrodes are nearby (small *m* values, see Fig. 2b), but like a pole–dipole array when current electrodes are far away from each other (large *m* values). The pPD-α deployment (Fig. 2c) is essentially a gradient array, but it behaves like a Wenner-Schlumberger array when the potential dipole is centred between the current electrodes, and like a pole–dipole array when the potential dipole is close to any of the current electrodes and *m* is large.

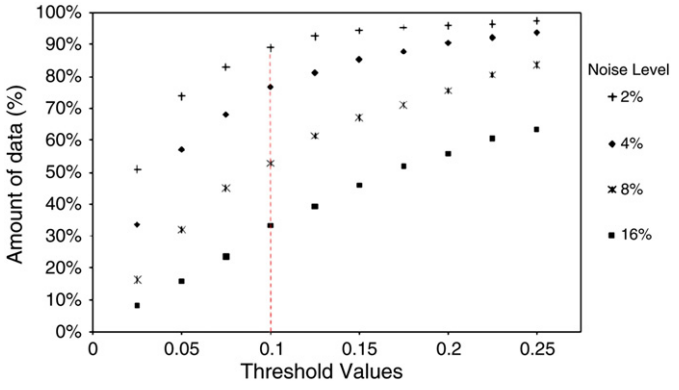

Fig. 6. Graph showing the amount of data that pass the proposed quality control through various threshold values. Noise levels of 2, 4, 8 and 16% have been taken into account.

3. Application

The proposed method allows dipole–dipole and Wenner-Schlumberger pseudosections to be obtained from two proposed datasets (pPD-β and pPD-α), using Eqs. (1) and (3). We have considered that the far electrode B is in-line, at a distance to the first electrode equal to the electrode spacing. We have called it pseudo pole–dipole array (pPD) because it is a four-electrode configuration. The values of *m* (Fig. 2b and c) will range from 1 to N − 2 for pPD-β array, and from N to 1 for the pPD-α. This allows the far location of the remote electrode to be avoided, which minimizes ambient (or geologic) noise sources and provides practical advantages.

A key question is the strategy used to assess the method, because the comparison between the directly measured dataset and the one computed from the pPD datasets can be useless if all datasets are affected by experimental errors. Thus, if there are discrepancies between datasets, the reason may lie not only in the method to be assessed, but also in data errors or static shift effects.

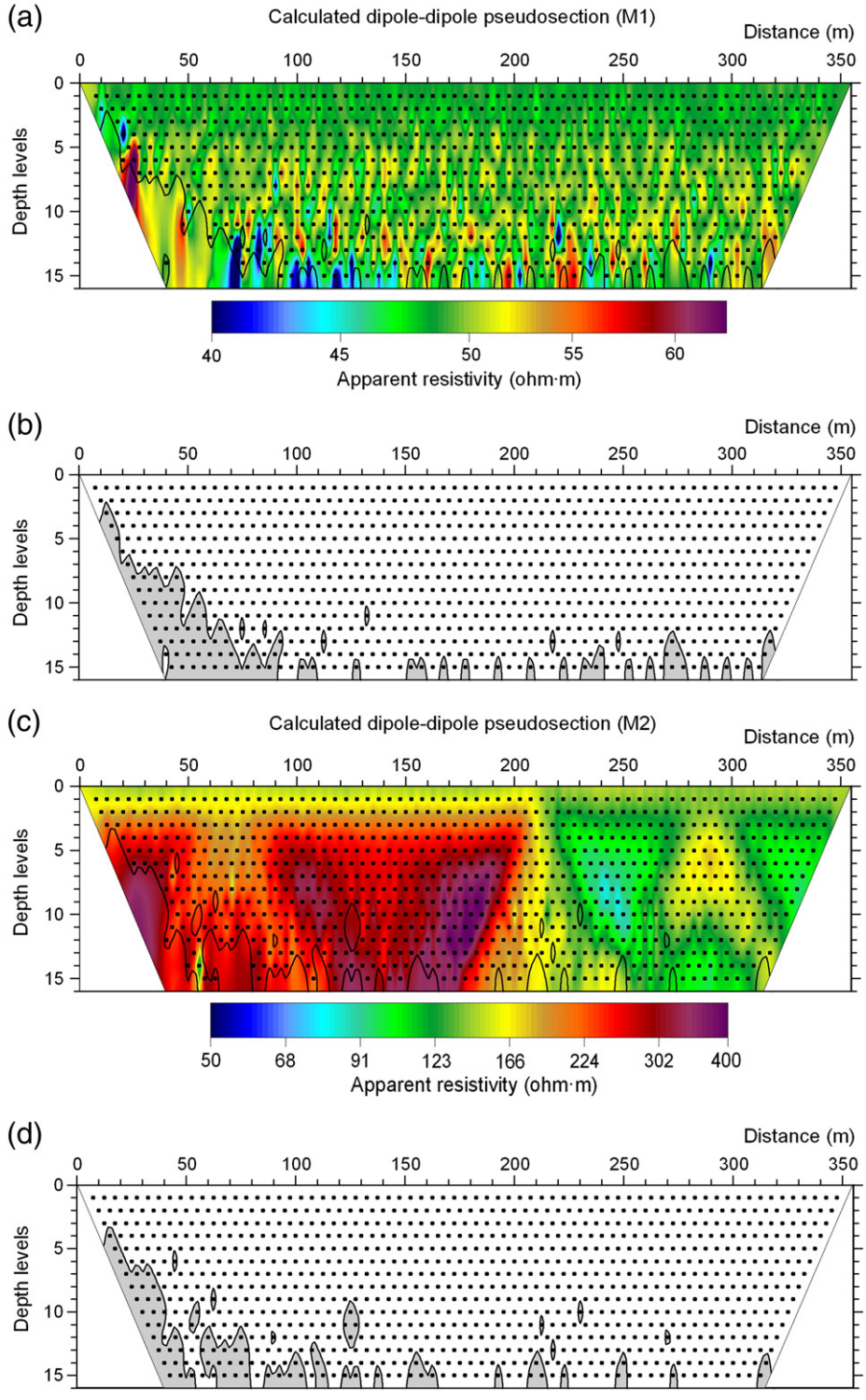

Fig. 7. Results obtained from Case 1 over dipole–dipole contaminated responses using a pseudosection representation. Calculated dipole–dipole apparent resistivity pseudosection from Eq. (1) for the model M1 (a) and M2 (c). Dipole–dipole pseudosections, (b) and (d), where the data that do not pass the proposed quality control have been coloured grey.

In this section, two scenarios are considered to take into account the abovementioned question. In the first one, model responses are contaminated by an additive noise to simulate the effect of experimental errors. This process enables the quality control to be introduced, which is possible to check because the (error-free) responses are known. In the second one, this quality control is applied to field datasets.

The synthetic datasets are built from the responses of two models, M1 and M2. The model M1 is a homogeneous halfspace of resistivity 50 Ωm. The model M2 consists of a 1 m-thick upper layer of resistivity 150 Ωm that overburdens a vertical contact between regions of resistivities100 Ωm and 400 Ωm, and various embedded square structures of resistivities 50 Ωm and 400 Ωm (Fig. 5). Dipole–dipole, Wenner-

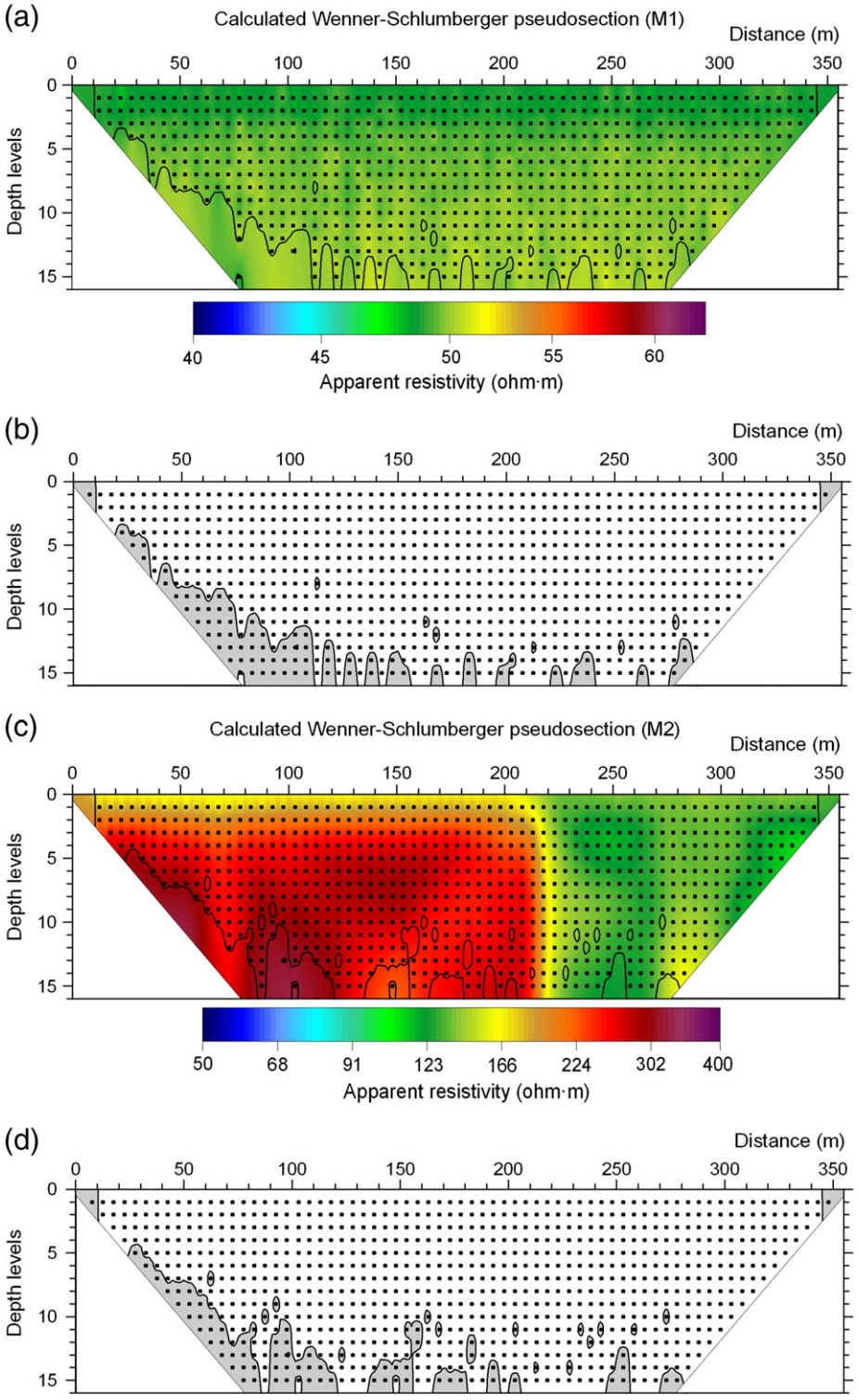

Fig. 8. Results obtained from Case 1 over Wenner-Schlumberger contaminated responses using a pseudosection representation. Calculated Wenner-Schlumberger apparent resistivity pseudosections from Eq. (2) for model M1 (a) and M2 (b). Wenner-Schlumberger pseudosections, (b) and (d), where data that do not pass the proposed quality control have been coloured grey.

Schlumberger and both pPD datasets, with 72 electrodes and an electrode spacing of 5 m, are computed from the two models. Model responses have been obtained using the code R2 (Binley, 2007).

When the Eqs. (1) and (2) are applied to error-free responses the relative differences between the calculated and the error-free responses are less than 10^{-4}.

The model responses are contaminated by adding a noise, ΔR, given by:

$$\Delta R = R\delta + \chi \tag{6}$$

where R is the error-free model response, and δ and χ are random numbers. δ follows a normal distribution with zero mean and standard deviation σ, and χ a uniform distribution in the interval $[-\varepsilon, +\varepsilon]$. These two random numbers (δ, χ) simulate the relative accuracy (δ) of the field data, and the instrumental resolution (χ). Values of 0.01, 0.02, 0.04, 0.08 for σ, and 10^{-5} V/A for ε have been considered.

3.1. Data Quality Control

The strategy followed to design the quality control (QC) has the advantage of having two independent pPD datasets, and of the fact that the dipole–dipole dataset can be computed from either of pPD deployments (pPD-α and pDP-β ones). Therefore, the QC can be established by comparing the two calculated dipole–dipole datasets. Because the pPD-α and the pDP-β are independent datasets, the QC can be considered equivalent to comparing normal and reciprocal measurements.

If the arithmetic mean between individually calculated dipole–dipole values is considered, $<R^{dd}>$ $(= 0.5[R_\alpha^{dd} + R_\beta^{dd}])$, the QC can be set according to the relative difference between this mean and the calculated value (R_α^{dd} or R_β^{dd}). This relative difference, ξ, is calculated as

$$\xi = \frac{\left|\langle R^{dd}\rangle - R_\alpha^{dd}\right|}{R^{dd}} = \frac{\left|\langle R^{dd}\rangle - R_\beta^{dd}\right|}{R^{dd}} = \frac{\left|R_\alpha^{dd} - R_\beta^{dd}\right|}{R_\alpha^{dd} + R_\beta^{dd}} \tag{7}$$

When the relative difference, computed by Eq. (7), is below an established threshold value, the pPD values used to compute R_α^{dd} and R_β^{dd} pass the QC.

The number of data that accomplish the QC depends on the noise and the established threshold value. In Fig. 6, this effect is explored considering the pPD-β deployment on the model M2. The noise level in the contaminated responses is mainly controlled by the relative accuracy and described by two standard deviations. The number of data that pass the QC through different threshold values and noise levels is plotted. For a threshold value equal to noise, the number of data that pass the QC is of 50%. From our own experience, a threshold

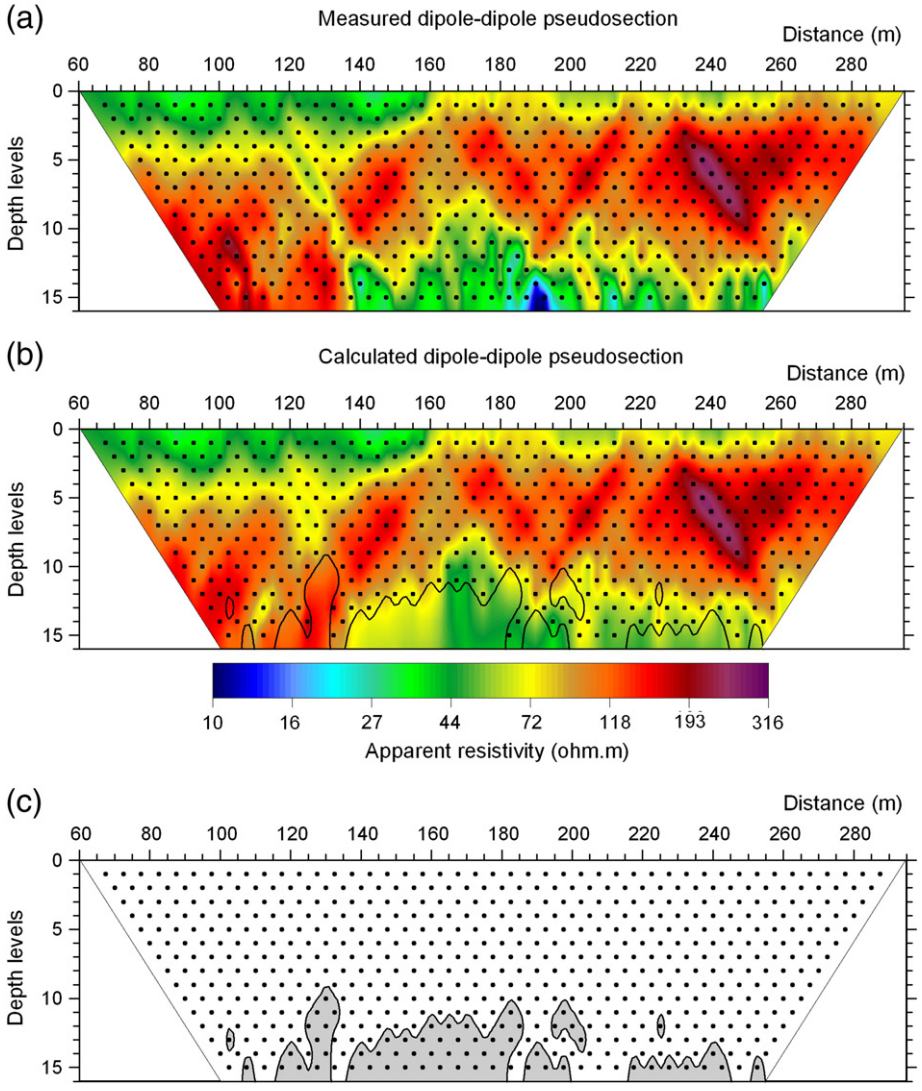

Fig. 9. Results obtained from Castellbisbal test site (Case 2) over dipole–dipole field datasets using a pseudosection representation. Measured (a) and calculated (b) dipole–dipole apparent resistivity from Eq. (1). Dipole–dipole pseudosection where data that do not pass the proposed quality control have been coloured grey (c) .

value of 0.1 has been taken, which ensures a reasonable number of reliable data (75% to 90%) for a noise level between 2% and 4%, that would be realistic for field data (Fig. 6). For the pPD-α dataset, the behaviour is equivalent.

Although the presented QC is based on the dipole–dipole dataset comparison, the pPD values that passed QC can also be used to obtain other datasets (e.g., the Wenner-Schlumberger one).

In summary, the method consists of four steps: 1- Computation of the dipole–dipole datasets from the two independent deployments, pPD-α and pPD-β. 2- Calculation of the relative differences between these two calculated datasets using Eq. (7). 3- Application of the quality control (QC) by setting a threshold value. The pPD values which relative differences, between computed dipole–dipole values, are below the threshold value are taken as reliable data. 4- Computation of the dataset of interest from the pPD data that have passed the QC.

4. Results

4.1. Case 1

In this case, contaminated model responses, from models M1 and M2, are used to test the application of the method. The results from contaminated dipole–dipole datasets are shown in Fig. 7. The dots in the pseudosections (a) and (c) indicate the dipole–dipole data calculated from the pPD data that passed the QC. The solid line confines the areas without computed values, because they are associated with data that do not pass the QC. In the pseudosections (b) and (d) all dipole–dipole data (dots) are presented, and the areas of the suspicious data are coloured grey. The QC has selected the 91% of the calculated dipole–dipole dataset.

Fig. 8 shows the calculated Wenner-Schlumberger datasets in the same way as Fig. 7. In this case, the QC has selected 90% of data as reliable.

4.2. Case 2

To test the practical implementation of the proposed method, a fieldwork was carried out at two different geological contexts: Castellbisbal and La Puebla de Roda test sites. Measurements were made using SYSCAL-Pro equipment (Iris Instruments, France) with a multichannel acquisition system. The profiles were acquired with the standard dipole–dipole and Wenner-Schlumberger, as well as the proposed pPD-α and pPd-β configurations.

4.2.1. Test site 1

The field test was carried out on an actual fluvial system. The test site was located in the riverbed of the lower Llobregat valley, in the

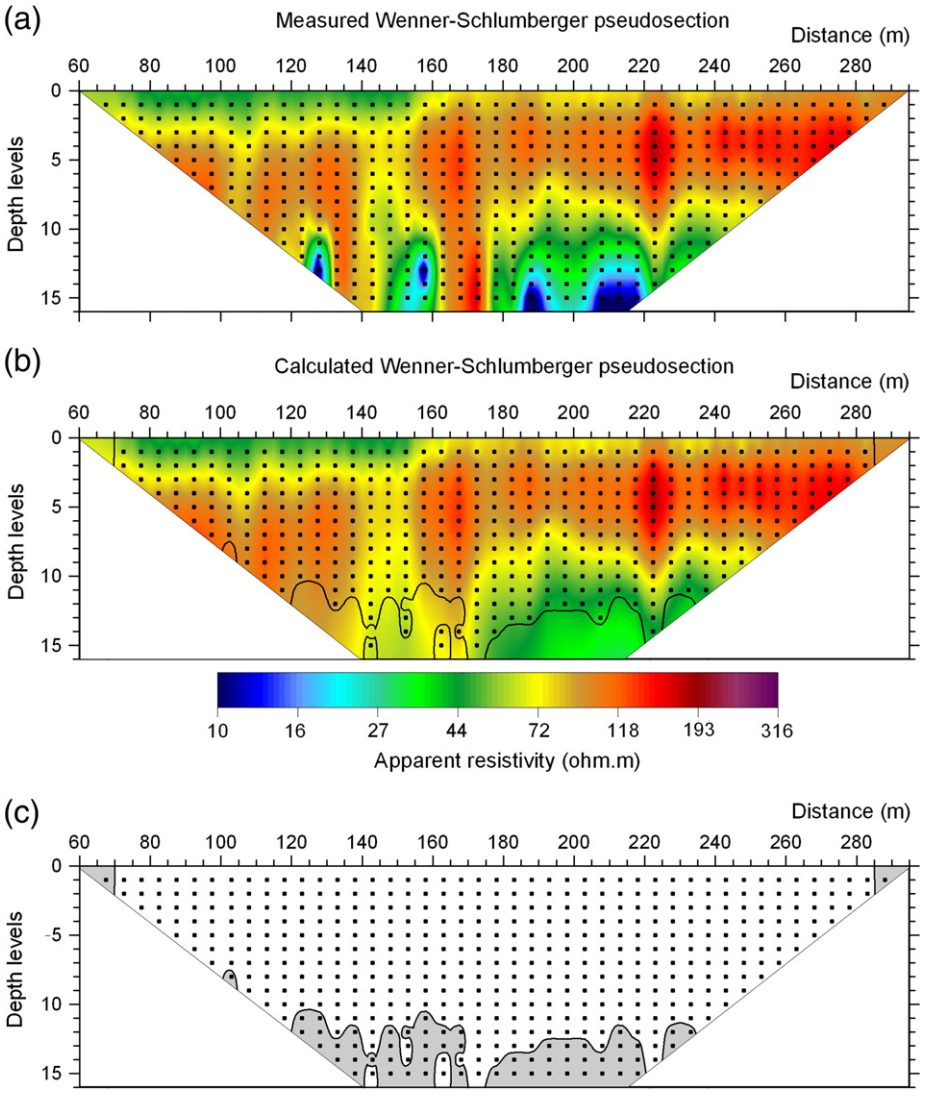

Fig. 10. Results obtained from Castellbisbal test site (Case 2) over Wenner-Schlumberger field datasets using a pseudosection representation. Measured (a) and calculated (b) Wenner-Schlumberger apparent resistivity from Eq. (2). Wenner-Schlumberger pseudosection where data that do not pass the proposed quality control have been coloured grey (c).

NW of Barcelona city, near Castellbisbal (Barcelona, Spain). Surface sediments are composed mainly of gravels and sands deposited in a fluvial system. All datasets were acquired along a 48-electrode profile with an electrode spacing of 5 m (total length 235 m).

Fig. 9 shows the directly measured dipole–dipole pseudosection and the one obtained following the proposed method. As in Case 1, the solid line in pseudosection (b) confines the areas without computed values, because they are associated to data that do not pass the QC. In pseudosection (c), all dipole–dipole data (dots) are presented, and the areas of the suspicious data are coloured grey. The results show that only the 11% of the calculated dipole–dipole data are not considered. Most of the doubtful data are located at the deepest levels of the pseudosection, which could be associated with a low signal-to-noise ratio.

Fig. 10 shows the measured and the calculated Wenner-Schlumberger datasets. The result shows that 12% of data are marked as doubtful, which is similar to the case of dipole–dipole.

Figs. 9 and 10 illustrate that the directly measured and the calculated pseudosections present a good fit.

4.2.2. Test site 2

This field test was carried out on the lower Eocene deltaic complexes of Roda Sandstone, near La Puebla de Roda (Huesca, Spain). These sediments are part of an ancient delta system (López-Blanco et al., 2003). The Roda Sandstone comprises an ensemble of essentially terrigenous deposits bounded by two prominent shallow-marine carbonate units. All configurations were recorded in a line with 72 electrodes and an electrode spacing of 0.5 m to attain an image of higher resolution over the prograding sandy delta front. Apparent resistivity pseudosections, with the directly measured and the calculated datasets, are presented in Figs. 11 (dipole–dipole pseudosections) and 12 (Wenner-Schlumberger pseudosections).

Results from La Pobla de Roda site show that only 2% of calculated dipole–dipole and Wenner-Schlumberger data are identified as doubtful. As in Test site 1, a very good fit between directly measured and calculated pseudosections is also shown.

5. Discussion and conclusions

The above results show that the calculated Wenner-Schlumberger pseudosections have a number of doubtful data similar to or greater than the calculated dipole–dipole ones. The reason is that the QC is based on dipole–dipole datasets comparison, which can be too restrictive to build the Wenner-Schlumberger dataset. The direct comparison between noise-free Wenner-Schlumberger model response (M2) and the one calculated from pPD data, without any QC, reveals that only 1% of calculated data presents relative differences higher than the

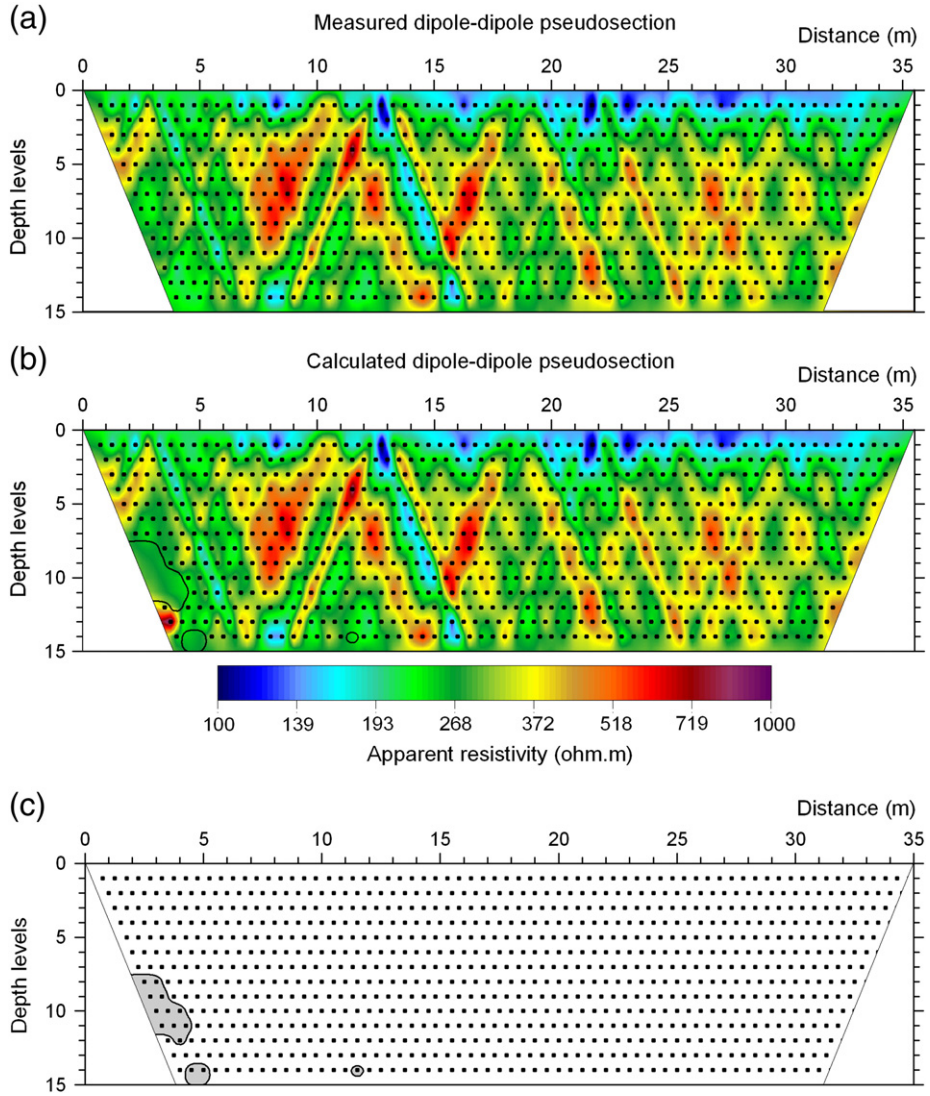

Fig. 11. Results obtained from La Puebla de Roda test site (Case 2) over dipole–dipole field datasets using a pseudosection representation. Measured (a) and calculated (b) dipole–dipole apparent resistivity from Eq. (1). Dipole–dipole pseudosection where data that do not pass the proposed quality control have been coloured grey (c).

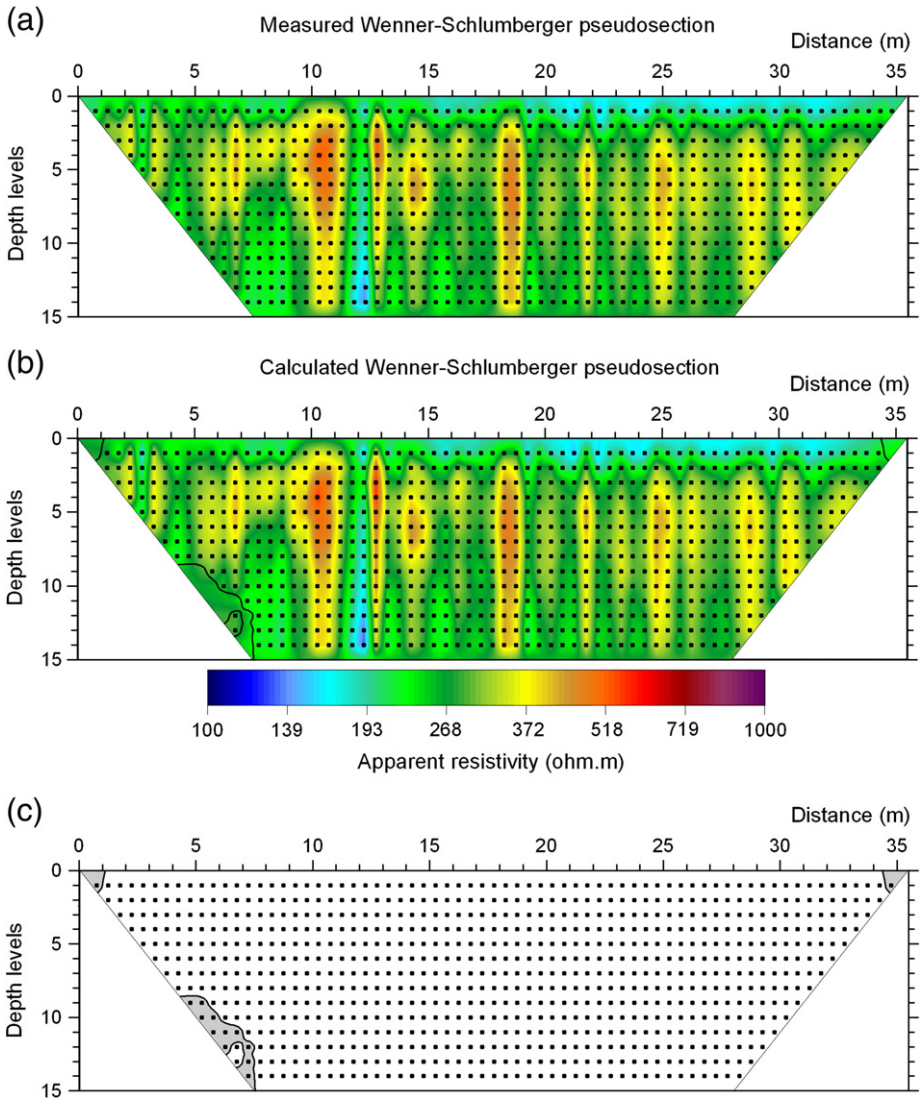

Fig. 12. Results obtained from La Puebla de Roda test site (Case 2) over Wenner-Schlumberger field datasets using a pseudosection representation. Measured (a) and calculated (b) Wenner-Schlumberger apparent resistivity from Eq. (2). Wenner-Schlumberger pseudosection where data that do not pass the proposed quality control have been coloured grey (c).

noise added (Fig. 13). Therefore, the computation of the Wenner-Schlumberger dataset seems to be less sensitive to the noise than the dipole–dipole one. This pattern is also valid for field data. This behaviour can be understood using an error propagation scheme: the calculation of Wenner-Schlumberger datasets involves an addition. Consequently when R_α and R_β values are similar in Eq. (3), the resultant R^{WS} is of the same order of magnitude, and its relative error is similar to the one of the pPD data. This is not necessarily true in the dipole–dipole datasets calculation, because the Eq. (1) involves a subtraction, and R^{dd} values can be much smaller than the pPD values, thus amplifying its relative error.

As a strategy for the Wenner-Schlumberger case, we propose using the QC only to identify the data that can be doubtful, and let the interpreter decide whether this data is reliable or not according to their own experience.

The results prove the applicability of the method to fieldwork datasets, and the validity of the introduced QC. In summary, the main features of the proposed method are:

- The pPD datasets can be transformed into other datasets in a straightforward way.
- The decision about the type of dataset to be used for interpretation can be delayed until (or even after) the interpretation time. Other datasets (not directly measured) can be obtained long after their acquisition if they are needed in further interpretations.
- The acquisition time of pPD sequences can be greatly reduced with a multichannel system, because this sequence is highly suitable for such instruments. The proposed configurations avoid the far location of the remote electrode, which is a great advantage to practical purposes.
- A data quality control based on the comparison between two independently calculated dipole–dipole datasets, similar to the normal and reciprocal measurements, is well established.

This method has been tested satisfactorily to reproduce dipole–dipole and Wenner-Schlumberger datasets, but it can be applied computing other datasets following the same scheme, e.g. the Wenner and the gradient arrays.

Acknowledgements

This work was partially supported by the Spanish Ministry of Science and Innovation and EU FEDER funds under projects CGL2007-66431-C02 and CGL2009-0760, and contract 2009SGR1198 from the Catalan Government.

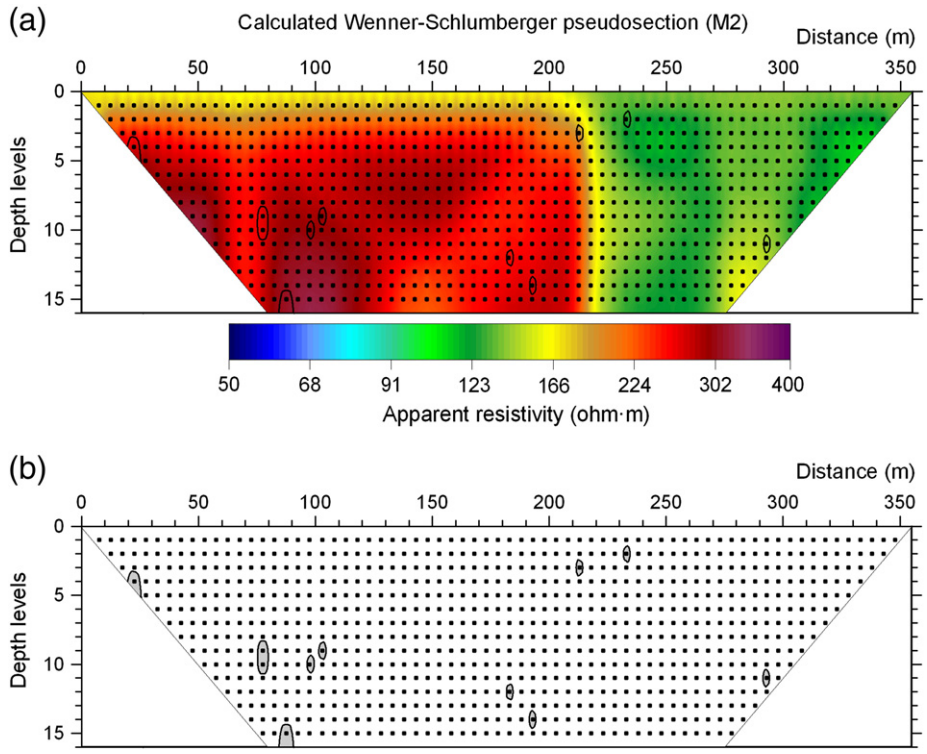

Fig. 13. Results obtained from direct comparison among measured and calculated Wenner-Schlumberger datasets using a pseudosection representation. Calculated Wenner-Schlumberger apparent resistivity without any quality control (a), and Wenner-Schlumberger pseudosection where data with relative differences higher than the noise added (2%) have been coloured grey (b).

Appendix A

In this appendix, a discussion about the number of injections required for multichannel instruments is presented for a dipole–dipole array, although the results may be equivalent to the pole–pole and pole–dipole arrays.

For a simple current injection, multichannel instruments allow recording as many simultaneous potential readings as the instrument has channels. This can help to reduce the acquisition time, which is proportional to the number of current injections in the array, as shown in Eq. (4).

The number of data of the pseudosection depends on the number of involved electrodes (e), and the number of desired levels (N). The maximum number of data of dipole–dipole pseudosection is

$$N_n = \frac{1}{2}(e-3)(e-2) \tag{A1}$$

In Fig. A1, the data distribution of the full pseudosection for a dipole–dipole with e-electrode array is shown. Crosses (x) correspond to data.

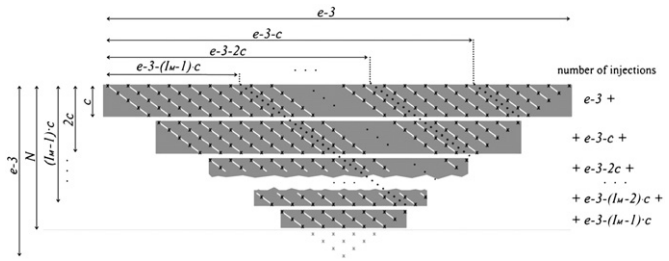

Fig. A1. Assignation point of data (x) in a dipole–dipole pseudosection. White lines connect points recorded simultaneously. Data points are grouped in bands of c levels. N is the number of levels; c is the number of channels, and I_M is the number of bands.

White lines represent data simultaneously measured for an injection with a multichannel system of c channels. The amount of injections will depend on e, N and c; its computation is based on the pseudosection of Fig. A1, where several bands can be also seen. Each (grey) band contains c levels except the one at the bottom that can contain less. The number of bands is denoted by I_M, which can be calculated by the expression

$$I_M = \mathrm{int}\left(\frac{N-1}{c}\right) + 1 \tag{A2}$$

where $int(x)$ corresponds to the integer part of x. I_M, also represents the maximum number of injections to reach the level N.

Each band involves a different number of injections, as can be seen in Fig. A1. The band on the top requires $e-3$ injections, but the following ones going down in the pseudosection need c injections lesser than the previous one. For the general case, the number of injections can be computed as

$$i = (e-3) + (e-3-c) + (e-3-2c) + \ldots + (e-3-kc) + \ldots + (e-3-[I_M-1]c)$$

This expression can be arranged in the following way to prove formula (5)

$$\begin{aligned} i &= \sum_{k=0}^{I_M-1}(e-3-kc) = \\ &= I_M(e-3) - c\sum_{k=0}^{I_M-1} k \\ &= I_M(e-3) - \frac{1}{2}c\{I_M(I_M-1)\} \\ &= I_M\left\{(e-3) - \frac{1}{2}c(I_M-1)\right\} \end{aligned} \tag{A3}$$

In the case of a monochannel instrument ($c=1$) the formula (A3) becomes

$$i=\frac{1}{2}N(2e-5-N), \tag{A4}$$

and if all the levels of the pseudosection are taken ($N=e-3$) in [A4], we obtain

$$i=\frac{1}{2}(e-3)(e-2)=N_n,$$

which coincides with the formula (A1).

References

Athanasiou, E.N., Tsourlos, P.I., Papazachos, C.B., Tsokas, G.N., 2007. Combined weighted inversion of electrical resistivity data arising from different array types. Journal of Applied Geophysics 62, 124–140.

Beard, L.P., Tripp, A.C., 1995. Investigating the resolution of IP arrays using inverse theory. Geophysics 60 (5), 1326–1341.

Binley, A., 2007. R2: 2-D inversion of resistivity data. Summary. Available from http://www.es.lancs.ac.uk/people/amb/Freeware/R2/R2_summary.htm (verified 17.06.10) Lancaster University, Lancaster, UK.

Candansayar, M.E., 2008. Two-dimensional individual and joint inversion of three- and four-electrode array dc resistivity data. Journal of Geophysics and Engineering 5, 290–300.

Candansayar, M.E., Basokur, A.T., 2001. Detecting small-scale targets by the 2D inversion of two-sided three-electrode data: application to an archaeological survey. Geophysical Prospecting 49, 13–25.

Carpenter, E.W., 1955. Some notes concerning the Wenner configuration. Geophysical Prospecting 3, 388–402.

Carpenter, E.W., Habberjam, G.M., 1956. A tri-potential method of resistivity prospecting. Geophysics 21, 455–469.

Coggon, J.H., 1973. A comparison of IP electrode arrays. Geophysics 38 (4), 737–761.

Dahlin, T., Zhou, B., 2004. A numerical comparison of 2D resistivity imaging with 10 electrode arrays. Geophysical Prospecting 52, 379–398.

Dahlin, T., Zhou, B., 2006. Multiple-gradient array measurements for multichannel 2D resistivity imaging. Near Surface Geophysics 113–123.

Habberjam, G.M., 1967. Short note: On the application of the reciprocity theorem in resistivity prospecting. Geophysics 32, 918.

Karous, M., Pernu, T.K., 1985. Combined sounding-profiling resistivity measurements with the three-electrode arrays. Geophysical Prospecting 33, 447–459.

LaBrecque, J.D., Miletto, M., Daily, W., Ramirez, A., Owen, E., 1996. The effects of noise on Occam's inversion of resistivity tomography data. Geophysics 61 (2), 538–548.

Loke, M.H., 2001. Electrical imaging survey for environmental and engineering studies. A practical guide to 2d and 3d survey. [On line]Available at http://www.terrajp.co.jp/lokenote.pdf2001(read of August 2010).

Loke, M.H., 2004. Tutorial: 2-D y 3-D electrical imaging surveys. [On line]Available at http://www.geoelectrical.com/coursenotes.zip2004(read of August 2010).

López-Blanco, M., Marzo, M., Muñoz, J.A., 2003. Low amplitude, synsedimentary folding of a deltaic complex: Roda Sandstone (lower Eocene) South-Pyrenean Foreland Basin. Basin Research 15, 73–95.

Parasnis, D.S., 1988. Reciprocity theorems in geoelectric and geoelectromagnetic work. Geoexploration 25, 177–198.

Van Nostrand, R.G., Cook, K.L., 1966. Interpretation of resistivity data: USGS. Prof. Pap. 499.

Xu, B., Noel, M., 1993. On the completeness of datasets with multielectrode systems for electrical resistivity survey. Geophysical Prospecting 41, 791–801.

Zhou, B., Dahlin, T., 2003. Properties and effects of measurements errors on 2D resistivity imaging surveying. Near Surface Geophysics 105–117.

Zhou, W., Beck, B.F., Adams, A.L., 2002. Effective electrode array in mapping karst hazards in electrical resistivity tomography. Environmental Geology 42, 922–928.

Publicació 2

Bellmunt F., Marcuello A., Ledo J., Queralt P., Falgàs E., Benjumea B., Velasco V., Vázquez-Suñé E., 2012. **Time-lapse cross-hole electrical resistivity tomography monitoring effects of an urban tunnel.** Journal of Applied Geophysics 87, 60–70.

Journal of Applied Geophysics 87 (2012) 60–70

Contents lists available at SciVerse ScienceDirect

Journal of Applied Geophysics

journal homepage: www.elsevier.com/locate/jappgeo

Time-lapse cross-hole electrical resistivity tomography monitoring effects of an urban tunnel

F. Bellmunt [a,*], A. Marcuello [a], J. Ledo [a], P. Queralt [a], E. Falgàs [a], B. Benjumea [b], V. Velasco [c,d], E. Vázquez-Suñé [c]

[a] Geomodels, Departament de Geodinàmica i Geofísica, Barcelona Knowledge Campus (BKC), Universitat de Barcelona, Martí i Franqués s/n, 08028 Barcelona, Spain
[b] Institut Geològic de Catalunya, IGC, Balmes, 209-211, 08006 Barcelona, Spain
[c] Departamento de Geociencias, Instituto de Diagnóstico Ambiental y Estudios del Agua (IDAEA-CSIC), Jordi Girona, 18, 08034 Barcelona, Spain
[d] GHS, Departamento de Ingeniería Geotécnica y Geociencias, Universitat Politécnica de Catalunya, BarcelonaTech, Jordi Girona 1-3 Edificio D-2, 08034 Barcelona, Spain

ARTICLE INFO

Article history:
Received 11 April 2012
Accepted 5 September 2012
Available online 14 September 2012

Keywords:
Electrical resistivity tomography (ERT)
Cross-hole apparent resistivity pseudosection
Tunnel boring machine
Experimental electrodes

ABSTRACT

Tunnel construction in urban areas has recently become a topic of interest and has increased the use of tunnel boring machines. Monitoring subsurface effects due to tunnel building in urban areas with conventional surface geophysical techniques is not an easy task because of space constraints. Taking advantage of the construction of a new metro line in Barcelona (Spain), a geoelectrical experiment, which included borehole logging and time-lapse cross-hole measurements using permanent electrode deployments, was designed to characterise and to study the subsurface effects of the tunnel drilling in a test site.

We present a case study in which the differences between time-lapse cross-hole resistivity measurements acquired before, during and after the tunnel drilling below the test site have been calculated using three different procedures: a constrained time-lapse inversion, a model subtraction and an inversion of the normalised data ratio. The three procedures have provided satisfactory images of the resistivity changes and tunnel geometry, but resistivity changes for the tunnel void were lower than predicted by modelling. This behaviour has been explained by considering a conductive zone around the tunnel.

Further, an apparent resistivity pseudosection for the cross-hole data, equivalent to the case of the equatorial dipole–dipole on the surface, is introduced.

1. Introduction

The new L9 line under construction in the Barcelona Metro network will link Barcelona International Airport and El Prat de Llobregat with the towns of Badalona and Santa Coloma de Gramenet through Barcelona. This construction project allowed the development of a case study to monitor the subsurface effects of tunnel drilling with a tunnel boring machine (TBM) in an urban area by integrating geological, hydrological and geophysical information. The present study is part of this project and involved applying geophysical methodologies to monitor the subsurface effects of the drilling process.

Tunnelling in urban areas with a TBM requires detailed geological knowledge of the materials that the tunnel goes through to adapt the TBM to local conditions and complete control of their effects on the subsoil in some areas (special buildings, hospitals, etc.). Before the tunnel drilling occurs, subsurface research is usually based on mechanical borehole data and soil tests, which improves the subsurface knowledge but only provides data in a single location. Geophysical surveys can help to extend this information and to obtain a better understanding of the affected subsurface volume to guide engineers, if required, in problematic areas.

Electrical resistivity tomography (ERT) with down-hole electrodes–single-hole ERT (SHERT) or cross-hole ERT (CHERT)–is widely used in engineering projects. Denis et al. (2002) proposed the re-use of boreholes previously drilled for geotechnical investigations for automatic monitoring of drillings with a TBM. Deucester et al. (2006) used 2D cross-hole resistivity tomography to design proper remedial actions below foundations. Gibert et al. (2006) used electrical tomography to monitor an excavation-damaged zone with rings of electrodes inside the tunnel. Chambers et al. (2007) used surface and cross-hole 3D electrical resistivity tomography for mineshaft imaging and Ha et al. (2010) used electrical resistivity techniques to detect weak and fracture zones during underground construction.

Compared with static surveys, geophysical time-lapse measurements also detail the dynamic changes in the subsurface properties, which can in turn provide insight into ongoing subsurface processes. In a particular sense, time-lapse CHERT enables the rate to be determined at which a particular process (e.g., controlled tracer injection) is occurring and the volume of the subsurface region affected to be defined (Barker and Moore, 1998; Cassiani et al., 2005; Miller et al., 2008; Oldenborger et al., 2007).

* Corresponding author.
E-mail address: fbellmunt@ub.edu (F. Bellmunt).

0926-9851/$ – see front matter © 2012 Elsevier B.V. All rights reserved.
http://dx.doi.org/10.1016/j.jappgeo.2012.09.003

The main goal of this case study is to use time-lapse CHERT measurements (acquired before, during and after the drilling) between two boreholes to identify subsurface changes caused by the tunnel drilling in an urban area. Moreover, borehole geophysical logs (natural gamma) were recorded to obtain better knowledge of the geology.

2. Test site geological and geophysical settings

To apply and develop geological, geophysical and hydrogeological methodologies over the future line L9 in the Barcelona Metro network, a test site was chosen in the Sant Cosme district, El Prat de Llobregat (Barcelona) (Fig. 1). This town is located on the right bank of the Llobregat River delta. Buildings and the infrastructure layout at the test site make it very difficult to design optimum geometries to work with surface geophysical techniques.

Geologically, the Llobregat delta is located between the Garraf and Collserola–Montnegre horst and the Barcelona half-graben. It is a depression controlled by faults and filled with pliocene and quaternary deposits. From a sedimentological point of view, the delta consists of two detrital complexes, the Lower Detrital Complex of Pleistocene age and the Upper Detrital Complex or Holocene delta (Marqués, 1984; Simó et al., 2005). The Holocene delta reaches a thickness of 60 m and lies over the Pleistocene paleochannel system, the thickness of which varies between 80 m and 15 m, thinning towards the NW.

The metro tunnel shaft was intended to pass through the Holocene delta complex at a depth of approximately 19 m with a tunnel diameter of 9.4 m. Therefore, two mechanical boreholes (named PA1 and PA2) were drilled to a depth of 30 m symmetrically to the tunnel trace (15 m apart from each other) to obtain detailed information about the geology and so that they could be used as piezometers (Fig. 2). The water table was located at a depth of 4 m. The borehole description identifies three main units, limited by stratigraphic discontinuities, different associated lithofacies (Lth.) and the superficial anthropic materials. The main units are described below.

- Delta plain, DP: composed mostly of brownish-grey clays interbedded with fine–very fine sands, Lth. A.
- Delta front, DF: characterised by a set of sediments that range from fine silty sands to coarse sands with some gravel layers, alternating with silty fine sand (Lth. B to H). They correspond to beach deposits and river channels. From a hydrogeological point of view, this is the shallow aquifer.
- Prodelta, Pd: consists mainly of clayey silts and fine sands, Lth. I. Towards the bottom, the unit becomes sandier (fine-sands). From a hydrogeological point of view, this unit would represent the aquitard.

The test site geophysical characterisation consisted of natural gamma (NG) logs acquired with a dual induction probe with a natural gamma ray sensor (Robertson Geologging Ltd.) sampled every 0.01 m at a logging speed of 3 m/min into each borehole. See Fig. 3 for a detailed description of each lithofacies and the NG logs. The geological description and NG logs are correlated: low NG values correlate with a low clay content and vice versa. The NG logs proved to be useful, especially in the test site characterisation, where the Lth. H (PA2), defined as medium-to-coarse sands and medium gravels from the borehole description (borehole core recovery was approximately 20%) seems to be clayey.

During the experiment, the water resistivity was also measured in the boreholes and its value remained at 1900 ± 100 μS/cm.

3. Experimental design

Home-made experimental electrodes and specific cables were produced for the CHERT measurements to monitor the tunnel drilling effects below the test site. As electrodes, stainless steel rectangular

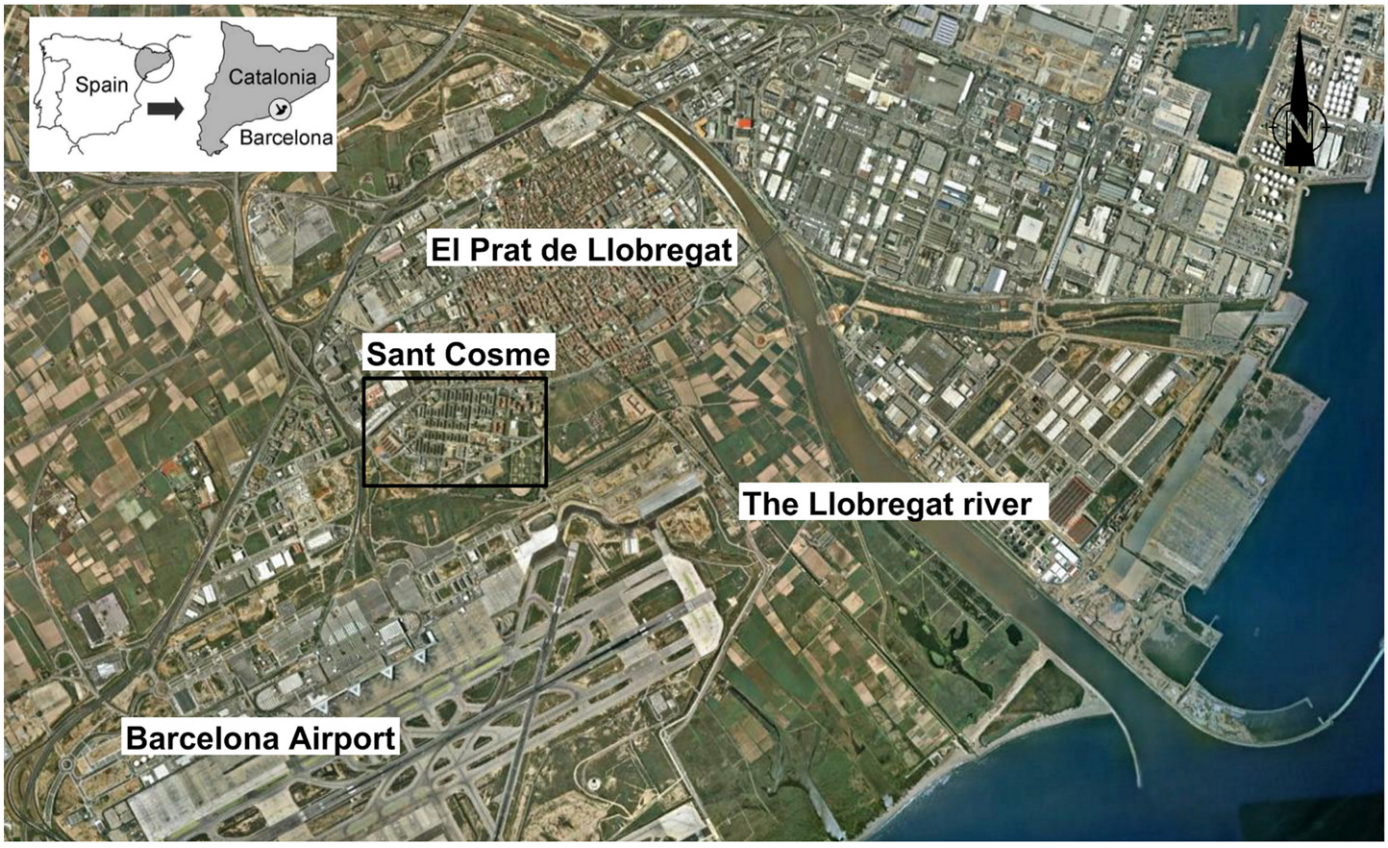

Fig. 1. Location of the test site (Sant Cosme district) in El Prat de Llobregat town (Barcelona, Spain).

meshes (0.1 m × 0.3 m) were directly fastened outside the PVC pipe during the piezometer installation, which avoided the borehole/borehole-fluid effects (Doetsch et al., 2010; Nimmer et al., 2008). Plastic-sheathed cables were attached outside the pipe and were connected to a Syscal Pro resistivity meter (Iris Instruments) by a standard connector (Fig. 4).

Due to the presence of anthropogenic materials up to a depth of 5 m and the position of the water table at a depth of 4 m, the first electrode was placed at a depth of 5 m. The PVC pipe was centred in each borehole and the small annular space between the pipe and borehole walls, consisting of poorly consolidated materials, provided us good electrode–ground contact. However, care had to be taken to prevent damage to the cables and electrode displacement during the installation of the PVC pipe.

Because of the small borehole annular space, the number of electrodes and the spacing chosen (24 electrodes evenly spaced 1 m from each other in each borehole) involved a trade-off between resolution and the desired borehole length to be monitored (see Fig. 5). The aspect ratio, or relation between the borehole separation and the total length of the instrumented borehole, should be no more than 0.75, ideally 0.5, to achieve better results in CHERT measurements (LaBrecque et al., 1996). In our case, CHERT measurements were acquired with an aspect ratio of 0.67 between the boreholes PA1 and PA2.

Before starting any geophysical measurement, subsoil conditions were allowed to stabilise for three weeks after the electrode installation. LaBrecque et al. (1996) observed that permanently installed electrodes were electrically noisier when first installed but that they improved over time. Later, conductivity logs with a dual induction probe were recorded in each borehole to supply the actual depth of each electrode because the stainless steel meshes used as electrodes created strong anomalies in the conductivity logs (not shown here). Due to the piezometer tubes included in the boreholes, which decrease in diameter in the slotted zones, the borehole geophysical logging did not reach the maximum possible depth. The conductivity log confirmed the spacing between electrodes because the electrodes were fixed to the casing prior to deployment into the boreholes. However, the electrode depths were corrected accordingly to avoid electrode mislocation effects on resistivity (Oldenborger et al., 2005; Wilkinson et al., 2008).

4. Monitoring the drilling effects on the test site

Monitoring the drilling effects consisted of time-lapse CHERT measurements acquired with the 48 electrodes installed into PA1 and PA2. The bipole–bipole (AM–BN) configuration (Zhou and Greenlangh, 1997, 2000) was the deployment used in this study.

Before the TBM passed through the test site, time-lapse CHERT datasets were acquired several days apart to identify possible anomalies correlated with the acquisition procedure, equipment or bad electrode contacts. Repeatability has also allowed us to calculate the background dataset and to estimate a data error of 1%.

The schedule of time-lapse CHERT measurements is presented in Table 1. The CHERT data acquisition was limited by the access to the test site.

4.1. Apparent resistivity pseudosection for CHERT data

The representation of the apparent resistivity is not a simple task with CHERT data because it involves more than two parameters (e.g., depth, level, orientation, etc.). In this paper, to have a rough image of the subsoil electrical structure, an apparent resistivity pseudosection equivalent to the case of the equatorial dipole–dipole on the surface has been built considering only data in which the current and potential electrodes A and M are at the same depth as the current and potential electrodes B and N, respectively. This

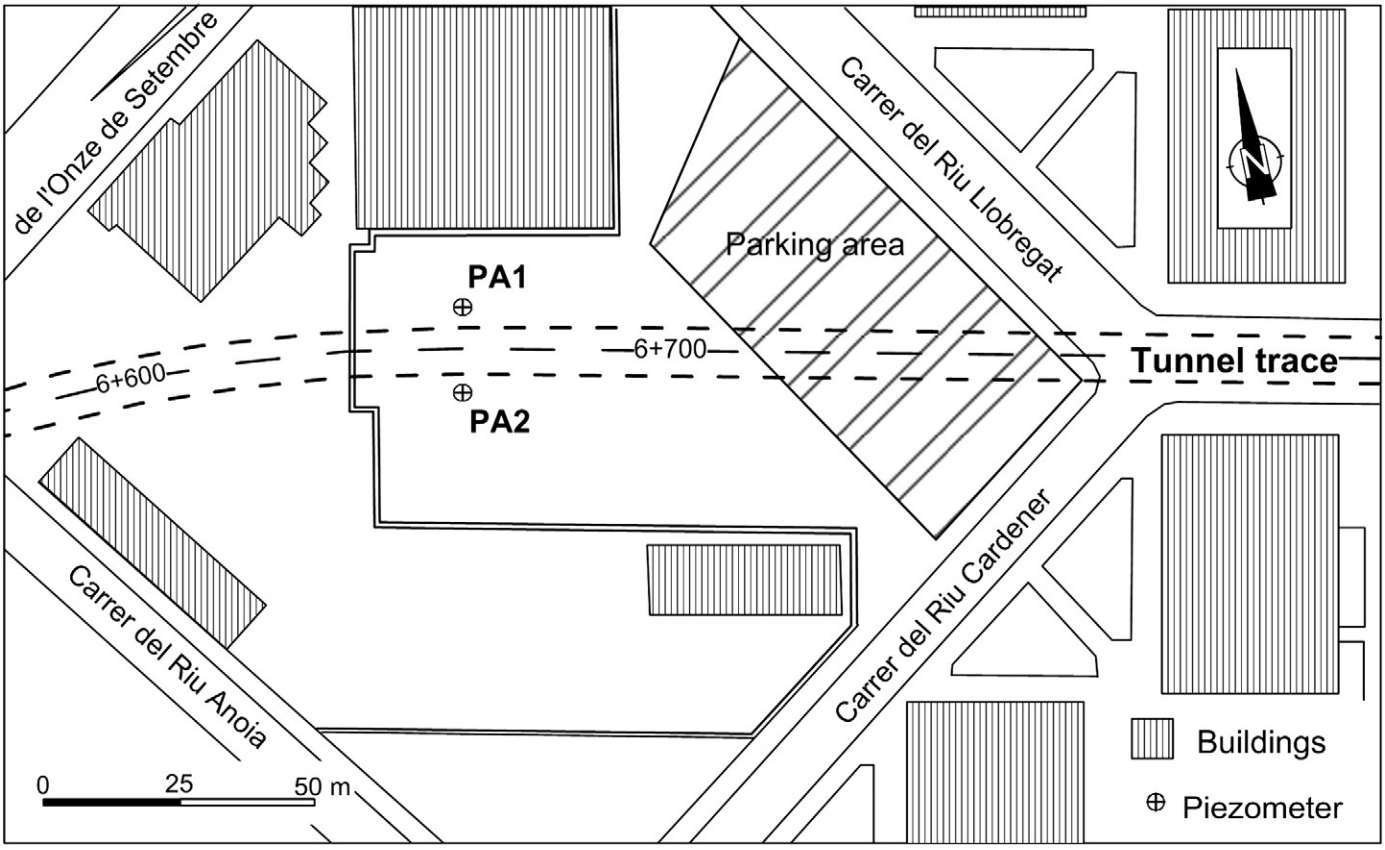

Fig. 2. Map of the test site showing the location of boreholes PA1 and PA2 and the tunnel trace. The tunnel goes from W to E.

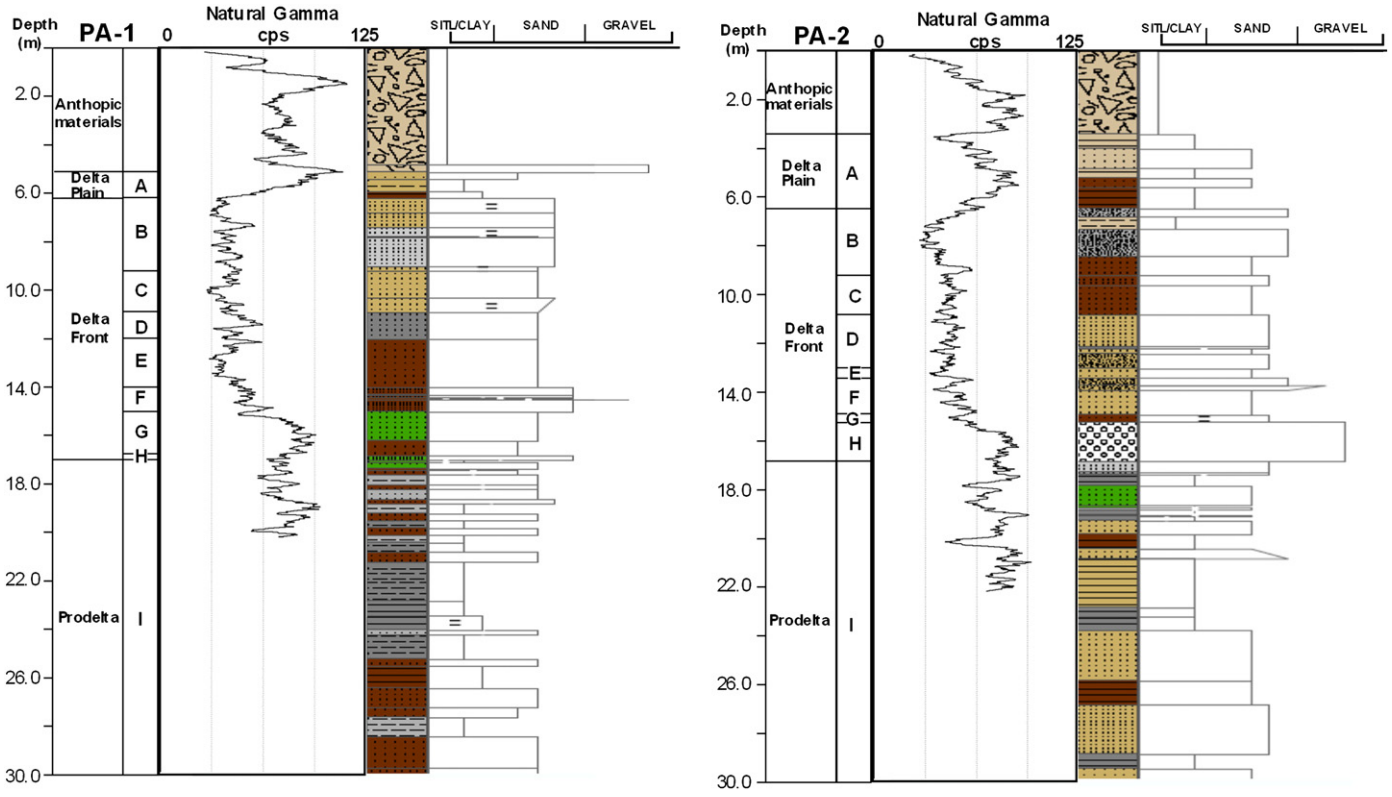

Fig. 3. Geological columns of boreholes PA1 and PA2 with the natural gamma logs. Survey points identified three main units and nine lithofacies (Lth.), which are repeated in almost all of the test sites: Delta plain (Lth. A: clay with fine–very fine sand), Delta front (Lth. B: medium sand interbedded with clay and silt, Lth. C: fine to very fine sand with clayey silt, Lth. D: medium to coarse sand with some gravel and clayey silt horizons, Lth. E: fine to very fine sand and clayey silt, Lth. F: medium to coarse sand interbedded with some gravel horizons, Lth. G: alternate layers of clayey silt and fine sand and Lth. H: medium to coarse sand and medium gravel), and Prodelta (Lth. I: clayey silt and fine sand). Natural gamma results are presented in cps (counts per second).

pseudosection only accounts for 12% of the recorded data for each dataset (Fig. 6).

Fig. 6A shows the apparent resistivity pseudosection when the TMB was drilling far from the test site (19th of March). A three-layer distribution can be observed: a resistive layer from 5.5 m down to 15.0 m (region a), a more conductive middle layer between 15 and 24 m (region b) and a more resistive layer at the bottom (region c). Fig. 6B and C corresponds to the apparent resistivity pseudosections on the 21st of March and the 16th of April, during and after the drilling underneath the test site, respectively. Fig. 6B shows a more conductive middle layer, which correlates to the effect of the TBM passing through it. Fig. 6C reveals a similar apparent resistivity distribution to that shown in Fig. 6A, but regions (b), (d) and (f) become more resistive, which points to the presence of the tunnel void.

4.2. Resistivity changes from time-lapse CHERT

The individual inversion of each time-lapse CHERT dataset has provided resistivity models in which the tunnel void and resistivity changes cannot be clearly identified. Therefore, three inversion procedures have been used to highlight them: a constrained time-lapse inversion (Loke, 2001), a model subtraction and an inversion of the normalised data ratio (Daily and Owen, 1991; Daily et al., 1992; Slater et al., 2000).

From our own experience, resistivity changes below 5% will not be considered in the model interpretation. This is consistent with the reported values of water resistivity during the experiment, which may produce subsoil resistivity variations up to ±5% according to Archie's law (Archie, 1942).

The reference model used for all three procedures (see Fig. 7) has been obtained after the inversion of the background dataset. The CHERT data do not seem to be able to identify each lithofacies within the main geological units. To make the location of the resistivity changes easily recognisable, we have established three zones (see Fig. 7) that may undergo changes in the resistivity: Zone 1 (between 5 m and 15 m), Zone 2 (between 15 m and 24 m) and Zone 3 (below 24 m).

4.2.1. Constrained time-lapse inversion

This procedure consists of using the first data set as a reference model to constrain the inversion of the later datasets. The robust smoothness constraint method has been used and the RMS obtained ranges from 0.9% to 1.9%. Resistivity changes are expressed in percentage by expression (1):

$$\%\Delta\rho = \left(\frac{\rho_i - \rho_0}{\rho_0}\right) \times 100 \quad (1)$$

where ρ_i is the resistivity of the model at time i and ρ_0 is the resistivity in the reference model. Positive values indicate that the model is becoming more resistive than the reference model, while negative values indicate a decrease in resistivity.

The images of the resistivity changes are presented in Fig. 8 (A to D). Fig. 8A shows that the resistivity values decreased by approximately 70% in the central part of Zone 2 while the TBM was drilling underneath the test site (21st of March at 14:52). At the same time, the resistivity increased by approximately 5%–10% in Zone 1 and in the left part of Zone 2. The resistivity variations tend to be accentuated during the drilling process through the test site, reaching values of 80% for a decrease in resistivity in the central portion of Zone 2 and of 10%–20% for an increase in resistivity in Zone 1 and Zone 3. The resistivity also increases by approximately 5%–10% near the electrodes in Zone 2 (Fig. 8B). Once the TBM left the test site (2nd and 16th of

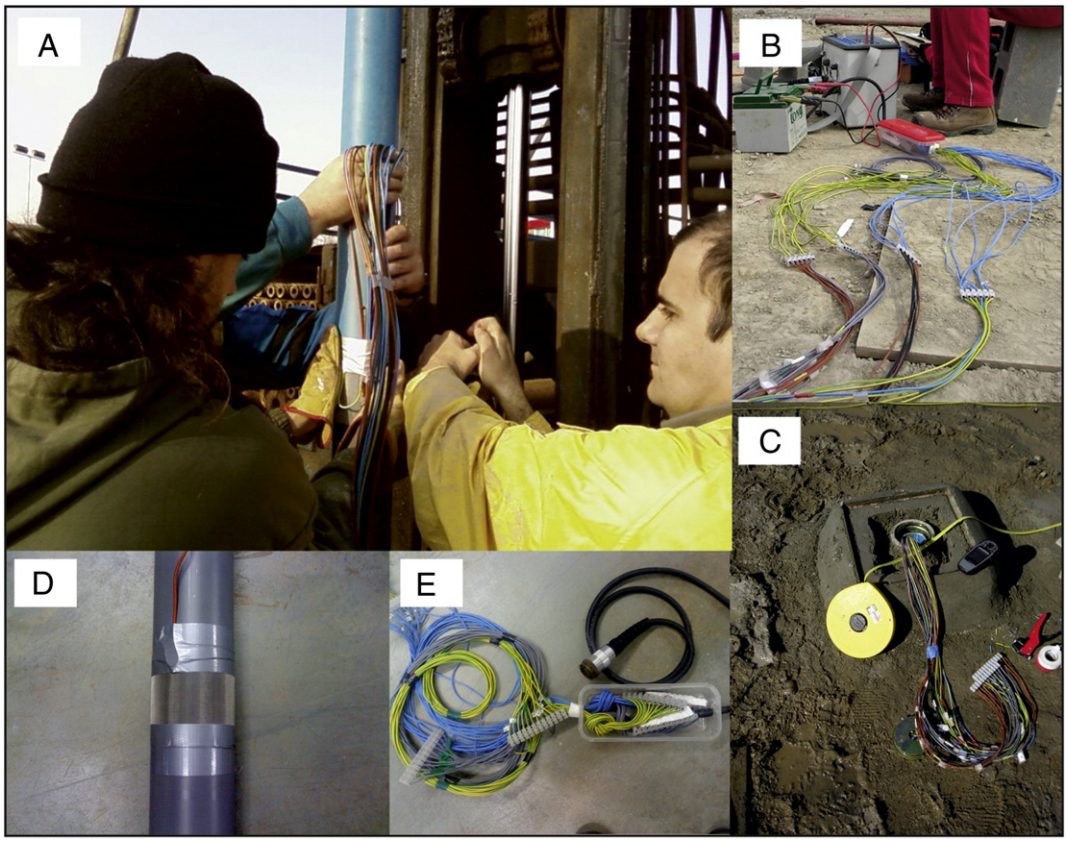

Fig. 4. Pictures of the piezometer equipment showing: (A) the installation of the meshes used as electrodes and cables, (B) and (C) the connexion with the resistivity meter and the external cables of the borehole and (D) and (E) details of the home-made meshes and connector.

April), the resistivity increased up to 70%–80% in central Zone 2 (Fig. 8C and D). Note that the resistivity increases by approximately 5%–10% around the tunnel void, especially above it (Fig. 8C and D).

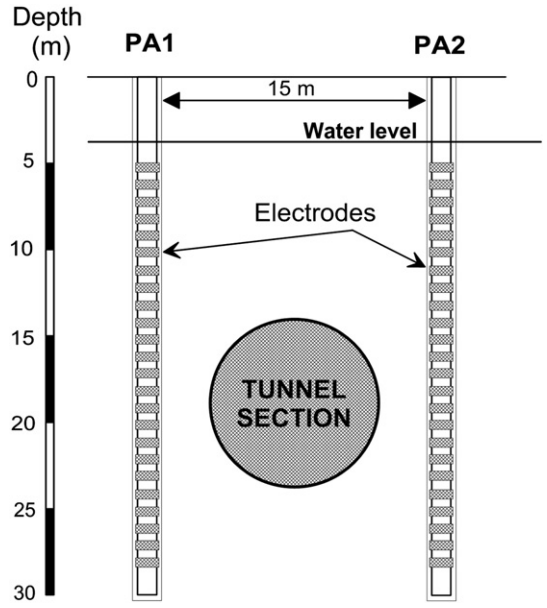

Fig. 5. Sketch of piezometers PA1 and PA2 with electrode locations and the water table. The tunnel section is also included.

4.2.2. Model subtraction

This procedure consists of calculating the resistivity changes after the individual inversion of each time-lapse dataset. The resistivity changes are expressed as percentage according to expression (1).

In this method, the application of the same inversion scheme to all the time-lapse datasets is required to make the comparison reliable. Among the different methods, the robust inversion method (Loke, 1999) was used because it shows a good resolution when sharp boundaries with strong resistivity contrast are involved. The RMS obtained in each individual inversion ranges from 0.7% to 1.2%. The resistivity changes obtained from the model subtraction method are presented in Fig. 9 (A to D).

During the tunnel drilling through the test site (21st of March at 14:52), the resistivity values decreased by approximately 75% in

Table 1
Schedule of geophysical measurements.

Date/time	Drilling conditions	Type of geophysical measurement
14/02/08	Piezometers equipped	
08/03/08		Geophysical borehole logging (dual induction probe)
12–13–14–19–20/03/08		CHERT-testing
21/03/08 14:52 h	TBM is passing through the test site	CHERT
21/03/08 19:53 h	TBM is passing through the test site	CHERT
02/04/08 12:17 h	Tunnel drilled	CHERT
16/04/08 11:49 h		CHERT

CHERT: cross-hole electrical resistivity tomography. TBM: tunnel boring machine.

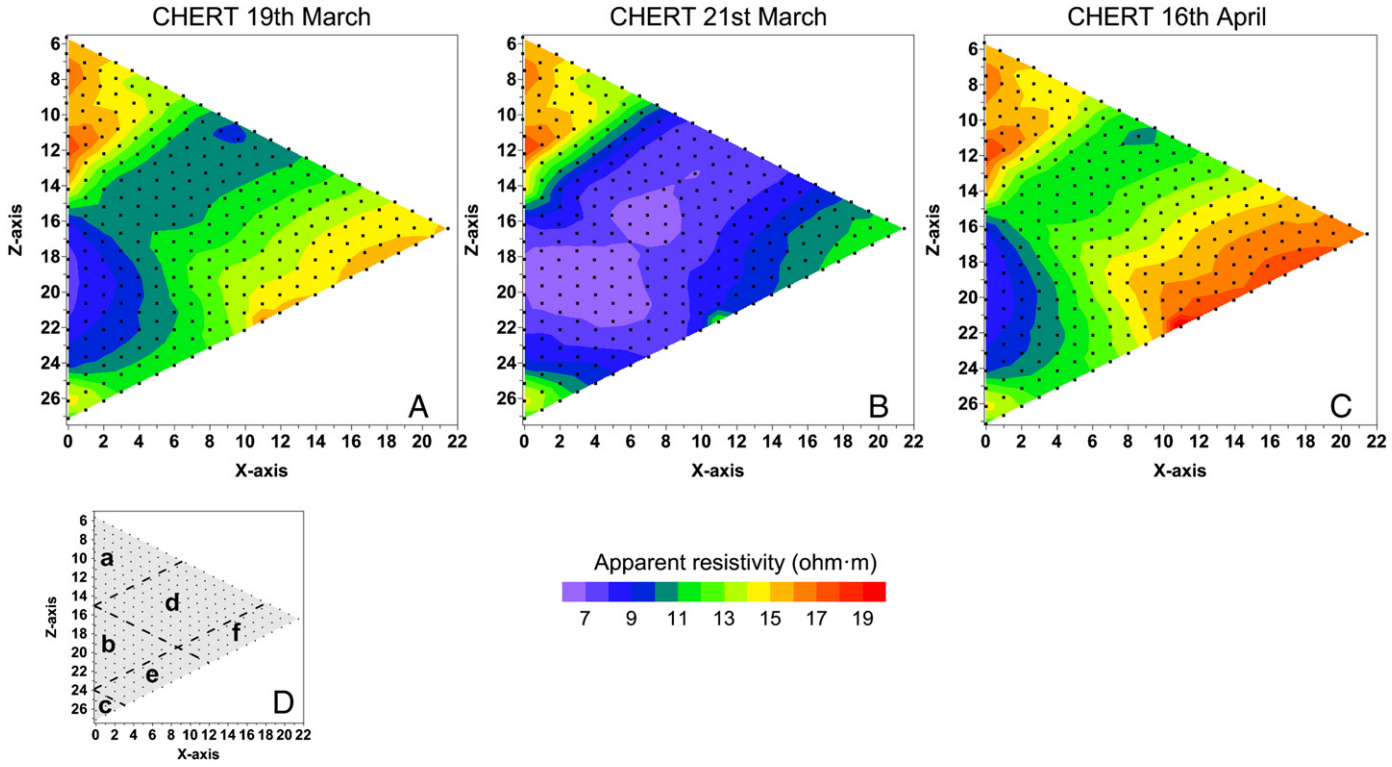

Fig. 6. Apparent resistivity pseudosections for cross-hole data. The axes are the midpoint depth between the AB and MN dipoles (z-axis) and the level $n-1$ (x-axis), which indicates the separation between dipoles. (A), (B) and (C) correspond to apparent resistivity pseudosections for the indicated dates and cross-hole data. (D) identifies the regions used in the pseudosection description. Regions (a), (b) and (c) correspond to the cases in which the two dipoles (AB and MN) are in the same layer. Regions (d), (e) and (f) correspond, respectively, to the cases in which one dipole is in the top layer and the other in the middle layer, in which one dipole is in the middle layer and the other dipole in the bottom layer and in which dipoles are on both top and bottom resistive layers.

central Zone 2 and increased by approximately 10%–20% in Zone 1 and on the left side of Zone 2 (Fig. 9A). These resistivity variations significantly increased over time, reaching a decrease in resistivity of 90% in central Zone 2 and increases of 20%–40% in Zones 1, 2 and 3 (Fig. 9B). Once the TBM left the test site (2nd of April and 16th of April), the resistivity increased up to 170% in central Zone 2 (Fig. 9C and D). Notice the high resistivity variations of approximately 10%–30% at the bottom of Zone 3, especially after the drilling.

4.2.3. Inverting the data ratio or normalisation

This procedure consists of inverting normalised datasets obtained by the following expression:

$$R_i^n = R_h\left(\frac{R_i^t}{R_0}\right) \tag{2}$$

where R_i^n is the normalised datum, R_0 is the background resistance value, R_i^t is the resistance value at time i and R_h is the theoretical resistance value for an arbitrary homogeneous resistivity distribution (e.g., 10 Ω·m). Note that Eq. (2) can work with apparent resistivity values and resistance values.

The inversion of a normalised dataset produces an image of resistivity changes relative to the homogeneous model. Therefore, subtle subsurface changes can be imaged using this approach (Daily et al., 2004). The robust inversion method was used and the RMS was in the range from 0.7% to 1.0%.

The changes in resistivity are presented as a percentage change in Fig. 10 (A to D). When the TBM was drilling through the test site (21st of March at 14:52), the resistivity decreased by approximately 80% in central Zone 2, but the resistivity increased by approximately 10%–20% in Zone 1 and by approximately 5%–10% on the left side of

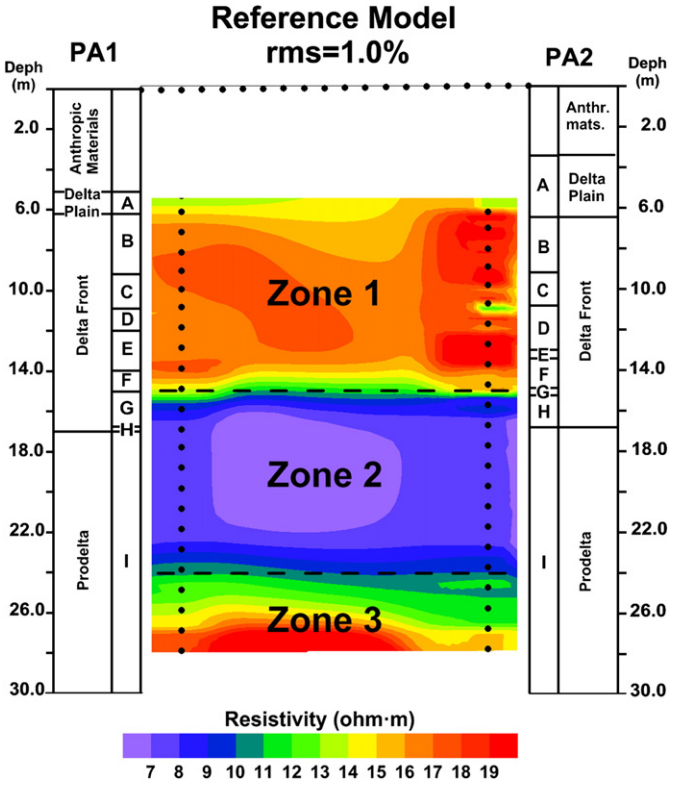

Fig. 7. Reference model obtained from CHERT measurements before the tunnel drilling through the test site. Geological units and lithofacies are also included. The horizontal dots correspond to topography and vertical dots to the electrode position.

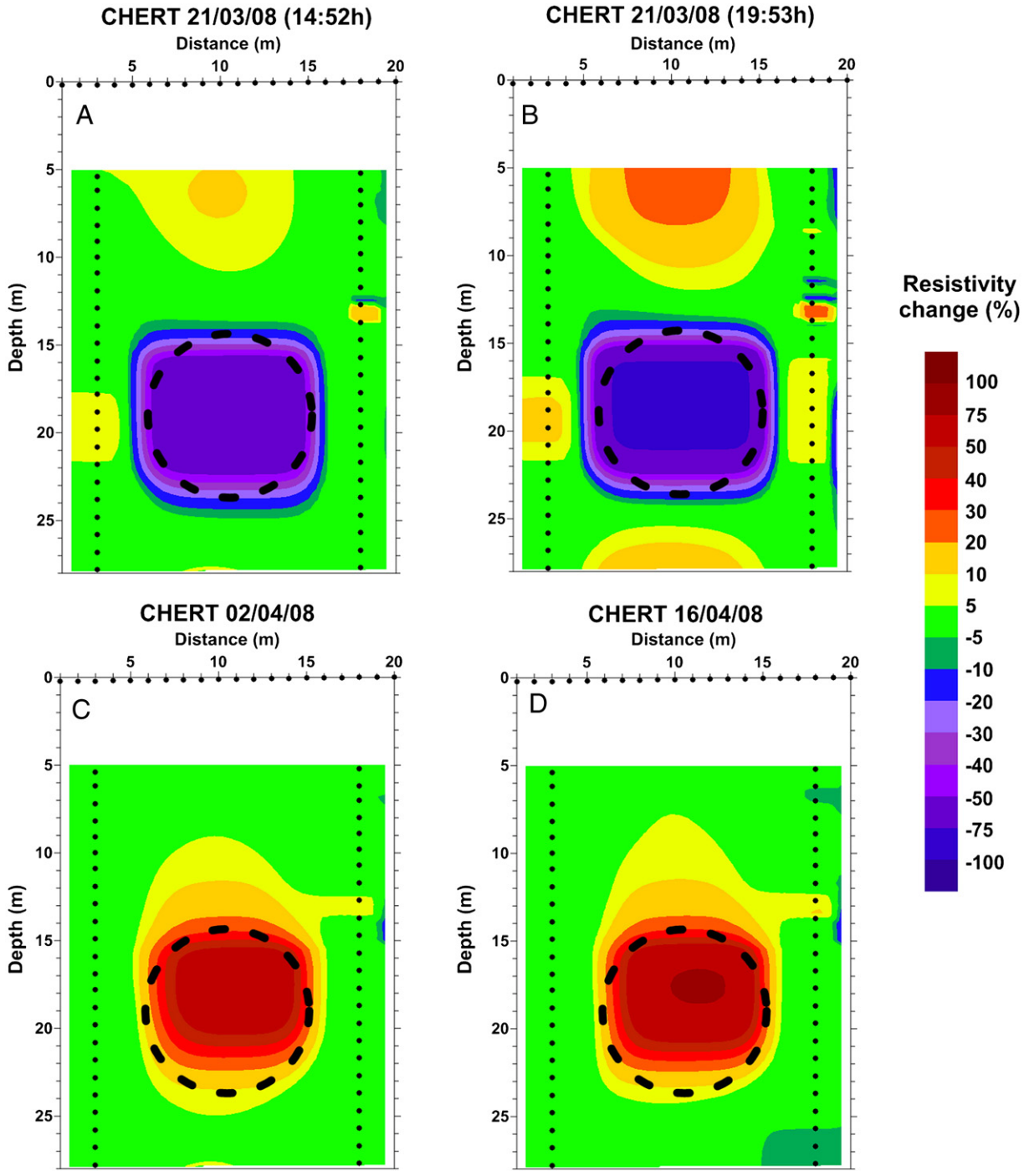

Fig. 8. Image sequence (A to D) of tunnel drilling considering the inversion with the robust smoothness constraint and by using Eq. (1). The dashed line corresponds to the tunnel section. The locations of the three areas identified that may suffer changes in the resistivity (Zone 1, Zone 2 and Zone 3) are included. See text.

Zone 2 (Fig. 10A). The resistivity changes increased over time, reaching values of 90% in central Zone 2 for the resistivity decrease and values for the resistivity increase of 20%–40% in Zone 1 and of 10%–20% in Zone 3 (Fig. 10B). Once the TBM left the test site (2nd of April and 16th of April), the resistivity increased up to 100% in central Zone 2. Moreover, the resistivity increases by approximately 10%–20% around the tunnel void (Fig. 10C and D).

5. Interpretation and discussion

In this study, all inversion procedures were consistent and showed a large decrease in resistivity in the central part of Zone 2 when the TBM was drilling through the test site (21st of March), whereas an increase in resistivity was detected at the same location once the TBM moved away from the test site (2nd of April and 16th of April). These variations are related to the presence of the TBM and to the tunnel void. Therefore, the tunnel section diameter can be satisfactorily estimated from the resistivity variation in the central portion of Zone 2. However, the resistivity changes for the tunnel void were lower than predicted by modelling. The maximum increase in resistivity at the tunnel depth was 80% caused by the robust smoothness constrained inversion, of 170% from the model subtraction procedure and 100% from the data ratio inversion procedure. This aspect will be discussed below.

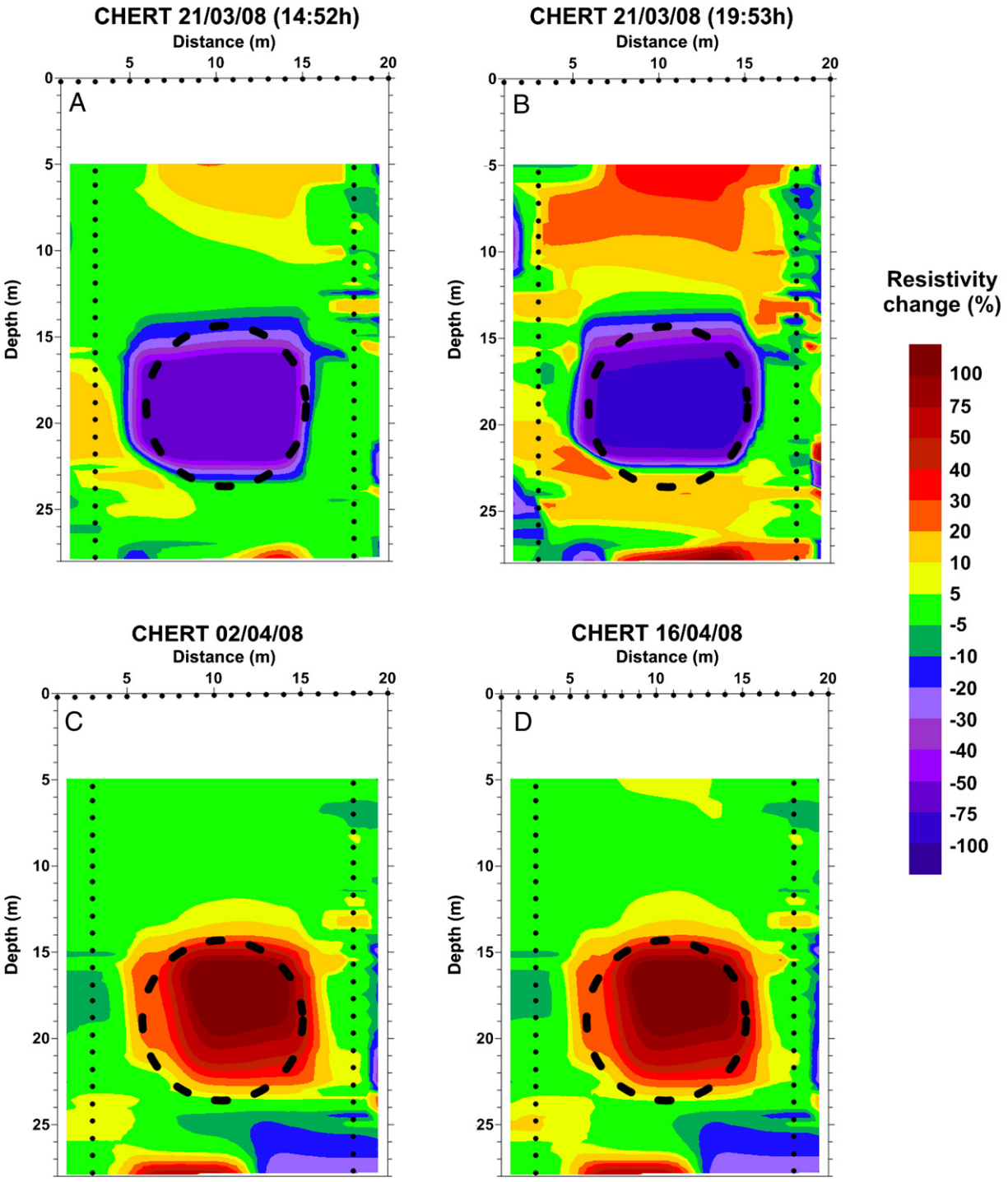

Fig. 9. Image sequence (A to D) of the difference between the resistivity models obtained by individual inversion and by using Eq. (1). The dashed line corresponds with the tunnel section. The locations of the three zones identified, which may suffer changes in the resistivity (Zone 1, Zone 2 and Zone 3), are included. See text.

To study this effect, we have simulated the tunnel void under the test site conditions and have calculated the resistivity variations using the three procedures mentioned above. The responses were non-distinguishable for a resistivity void contrast higher than 300 times that of the surroundings. In this case, we have taken a value of 10,000 Ω·m for the tunnel resistivity. The resistivity variations related to the presence of the tunnel void are significantly higher than the ones calculated from field datasets. For this reason, following Suzuki et al. (2004), a conductive zone of 3 Ω·m and a thickness of 1 m around a tunnel void has been simulated. In this case, the calculated resistivity changes are similar to the ones calculated from field datasets (see Fig. 11), suggesting the need for this conductive zone around the tunnel void, whose origin is not clear when drilling soft soils. This zone could have been produced by changes in the physical properties or the water content of the materials around the tunnel void, such as an increasing of the porosity in the materials surrounding the tunnel due to relaxation of the subsoil after drilling or an effect due to the injection of viscous fluids around the shield simultaneous with the advancement of the TBM.

The other relevant resistivity changes identified by comparing the resultant images obtained by each inversion procedure are presented and discussed below. First, the resistivity increased in almost all zones

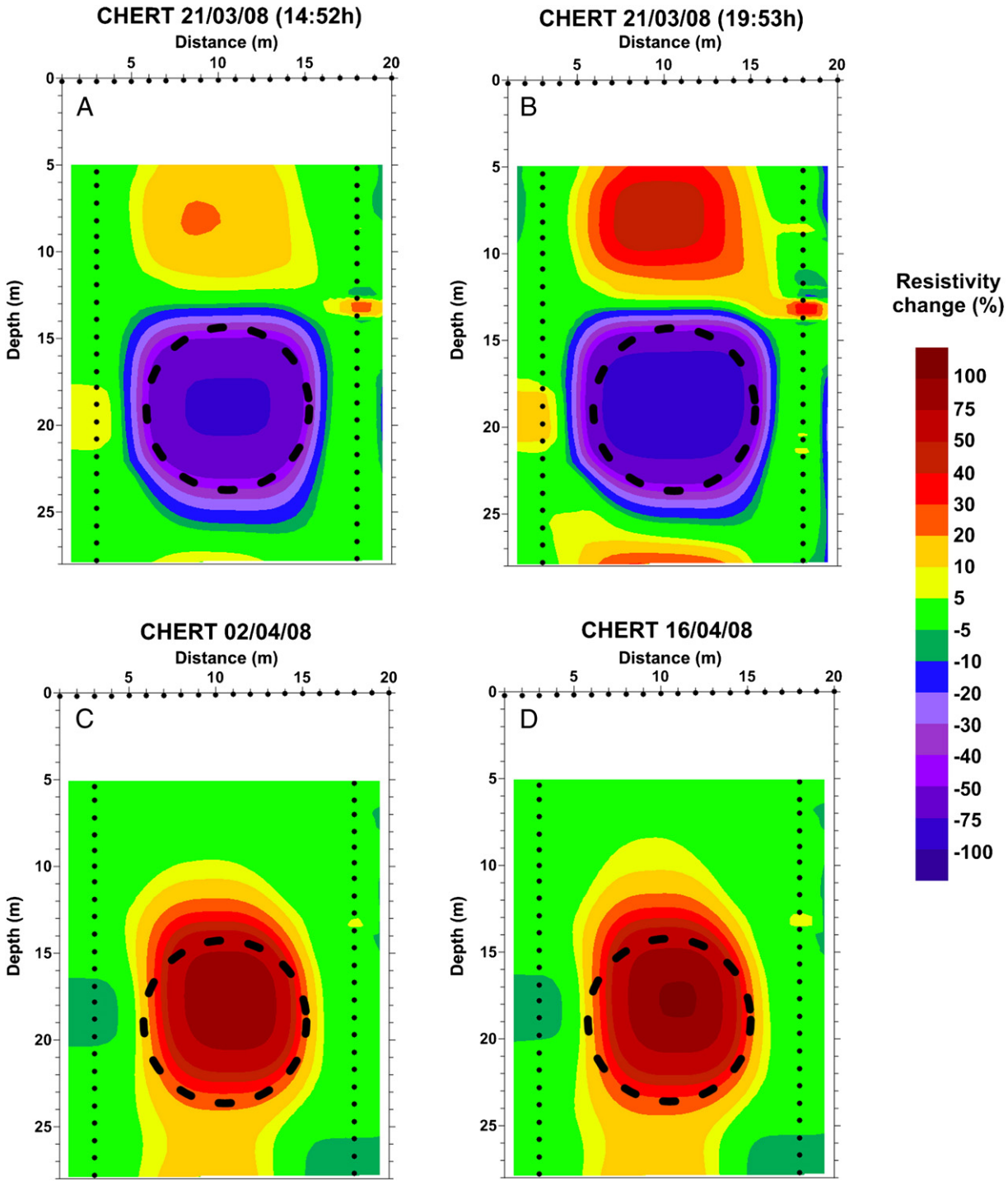

Fig. 10. Image sequence (A to D) of tunnel drilling considering the inversion of the normalised data ratio given by Eq. (2). The dashed line corresponds to the tunnel section. The location of the three areas identified, which may suffer changes in the resistivity (Zone 1, Zone 2 and Zone 3), are included. See text.

of the models during the tunnel drilling through the test site using the three procedures, but it was slightly higher in the case of the ratio procedure and much higher in the case of model subtraction. Second, high resistivity variations near the electrodes were detected in the model subtraction images, although the ones obtained from the other two procedures are almost free of them.

The variations in resistivity seem to be more scattered in the model subtraction images. Notice that slight differences in the individual data fitting of each dataset can result in different resistivity values in the resulting models. Therefore, the resistivity variations near the electrodes and in the bottom of Zone 3 can be associated with undesired effects due to the individual inversion of each dataset.

6. Conclusions

We have shown that CHERT can be used as a "quasi-real time" tool to detect possible anomalous situations in drilling contexts with TBM in urban areas. In addition, permanently installed electrodes facilitate long-term monitoring of subsurface structures, such as tunnels, to monitor possible unexpected damage. We consider the CHERT method with the experimental electrodes and cables to be a rapid and cost-effective tool for monitoring the subsoil effects due to engineering subsurface processes in urban areas. We have also shown that geophysical logs can help to better characterise the geology of the test site.

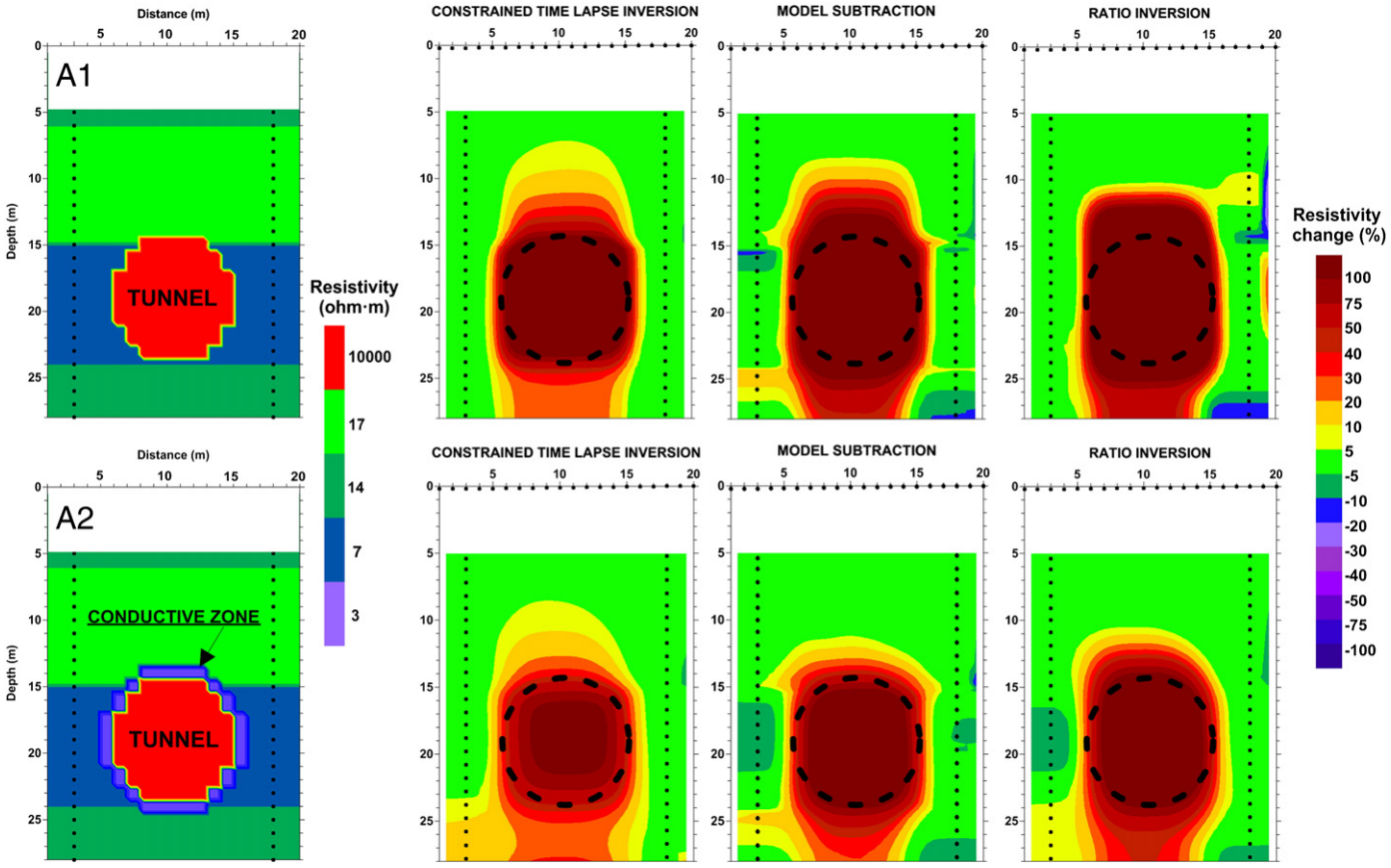

Fig. 11. Synthetic models of a tunnel void as a resistive zone (A1), taking into account a conductive zone around the void (A2) under the test site conditions. Change models are obtained from each model (A1 and A2) using three procedures: constrained time-lapse inversion, model subtraction and inversion of a normalised ratio.

We found that it was of utmost importance to acquire repeated datasets before starting any process at the test site to obtain a background dataset and to estimate the data error.

The comparison of the three procedures, along with the use of modelling, has been quite helpful in identifying the most relevant changes and artefacts and in justifying the low resistivity values through the presence of a conductive zone around the tunnel. Further studies would be needed to interpret this conductive zone around the tunnel in soft soils and the resistivity changes observed during tunnel drilling in Zones 1 and 3.

The apparent resistivity pseudosection for cross-hole data, equivalent to the case of the equatorial dipole–dipole on the surface, exhibits the main features of the resistivity variations along time lapse sequences.

Acknowledgements

This project was supported by the Spanish Ministry of Science and Innovation and EU FEDER funds under contract projects HEROS (CGL2007-66748), PIERCO2 (CGL2009-07604) and MEPONE (BIA2010-20244), by the Spanish Ministry of Industry (programme PROFIT 2007–2009) under project GEO-3D, and by the Ibero-American Science and Technology for Development Programme (CYTED), Project P711RT0278. We also thank the two anonymous reviewers for their helpful comments.

References

Archie, G.E., 1942. The electrical resistivity log as an aid in determining some reservoir characteristics. Petroleum Transactions of AIME 146, 54–62.
Barker, R., Moore, J., 1998. The application of time-lapse electrical tomography in groundwater studies. The Leading Edge 17, 1454–1458.
Cassiani, G., Bruno, V., Villa, A., Fusi, N., Binley, A.M., 2005. A saline trace test monitored via time-lapse surface electrical resistivity tomography. Journal of Applied Geophysics 59 (3), 244–259.
Chambers, J.E., Wilkinson, P.B., Weller, A.L., Meldrum, P.I., Ogilvy, R.D., Caunt, S., 2007. Mineshaft imaging using surface and crosshole 3D electrical resistivity tomography: a case history from the East Pennine Coalfield, UK. Journal of Applied Geophysics 62, 324–337.
Daily, W., Owen, E., 1991. Cross-borehole resistivity tomography. Geophysics 56, 1228–1235.
Daily, W., Ramirez, A., LaBrecque, D., Nitao, J., 1992. Electrical resistivity tomography of vadose water movement. Water Resources Research 28 (5), 1429–1442.
Daily, W., Ramirez, A., Binley, A.M., LaBrecque, D., 2004. Electrical resistance tomography. The Leading Edge 23 (5), 438–442.
Denis, A., Marache, A., Obellianne, T., Breysse, D., 2002. Electrical resistivity borehole measurements: an application to an urban tunnel site. Journal of Applied Geophysics 50, 319–331.
Deucester, J., Delgranche, L., Kaufmann, O., 2006. 2D cross-borehole resistivity tomographies below foundations as a tool to design proper remedial actions in covered karst. Journal of Applied Geophysics 60, 68–86.
Doetsch, J.A., Coscia, I., Greenhalgh, S., Linde, N., Green, A., Günter, T., 2010. The borehole-fluid effects in electrical resistivity imaging. Geophys. 75 (4), F107–F114.
Gibert, D., Nicollin, F., Kergosien, B., Bossart, P., Nussbaum, C., Grislin-Mouëzy, A., Conil, F., Hoteit, N., 2006. Electrical tomography monitoring of the excavation damaged zone of the Gallery 04 in the Mont Terri rock laboratory: field experiments, modelling and relationship with structural geology. Applied Clay Science 33, 21–34.
Ha, H.S., Kim, D.S., Park, I.J., 2010. Application of electrical resistivity techniques to detect weak and fracture zones during underground construction. Environmental Earth Sciences 60, 723–731.
LaBrecque, D.J., Ramirez, A.L., Daily, W.D., Binley, A.M., Schima, S.A., 1996. ERT monitoring of environmental remediation processes. Measurement Science and Technology 7, 375–383.
Loke, M.H., 1999. Time-lapse resistivity imaging inversion. Proceedings of the 5th Meet. Environ. Eng. Geophys. Soc. Eur. Sect., Em1. [On line]. Available at http://geoelectrical.com/timeabs.pdf, read of March 2011.
Loke, M.H., 2001. Constrained time lapse resistivity imaging inversion. The Environmental and Engineering Geophysical Society SAGEEP 2001 Symposium Program, March 2001, Denver, 34.
Marqués, M.A., 1984. Les formacions Quaternaries del Delta del Llobregat. Ed. Inst. Estud. Catalans, Barcelona.
Miller, C.R., Routh, P.S., Brosten, T.R., McNamara, J.P., 2008. Application of time-lapse ERT imaging to watershed characterization. Geophys. 73 (3), 7–17.

Nimmer, R.E., Osiensky, J.L., Binley, A.M., Williams, B.C., 2008. Three-dimensional effects causing artifacts in two-dimensional, cross-borehole, electrical imaging. Journal of Hydrology 359, 59–70.
Oldenborger, G.A., Routh, P.S., Knol, M.D., 2005. Sensitivity of electrical resistivity tomography data to electrode position errors. Geophysical Journal International 163, 1–9.
Oldenborger, G.A., Knoll, M.D., Routh, P.S., LaBrecque, D.J., 2007. Time-lapse ERT monitoring of an injection/withdrawal experiment in a shallow unconfined aquifer. Geophys. 72 (4), 177–187.
Simó, J.A., Gàmez, D., Salvany, J.M., Vàzquez-Suñé, E., Carrera, J., Barnolas, A., Alcalá, F.J., 2005. Arquitectura de facies de los deltas cuaternarios del río Llobregat, Barcelona, España. Geogaceta 38, 171–174.
Slater, L.D., Binley, A.M., Daily, W., Johnson, R., 2000. Cross-hole electrical imaging of a controlled saline tracer injection. Journal of Applied Geophysics 44, 85–102.
Suzuki, K., Nakata, E., Minami, M., Hibino, E., Tani, T., Sakakibara, J., Yamada, N., 2004. Estimation of the zone of excavation disturbance around tunnels, using resistivity and acoustic tomography. Exploration Geophysics 35, 62–69.
Wilkinson, P.B., Chambers, J.E., Lelliott, M., Wealthall, G.P., Ogilvy, R.D., 2008. Extreme sensitivity of crosshole electrical resistivity tomography measurements to geometric errors. Geophysical Journal International 173, 49–62.
Zhou, B., Greenlangh, S.A., 1997. A synthetic study on cross-hole resistivity imaging with different electrode arrays. Exploration Geophysics 28, 1–5.
Zhou, B., Greenlangh, S.A., 2000. Cross-hole resistivity tomography using different electrode configurations. Geophysical Prospecting 48, 887–912.

Publicació 3

Bellmunt F., Marcuello A., Ledo J., Queralt P., 2015. **Capability of cross-hole electrical configurations for monitoring rapid plume migration experiments.** Actualment en revisió en la revista Journal of Applied Geophysics.

Elsevier Editorial System(tm) for Journal of Applied Geophysics
Manuscript Draft

Manuscript Number: APPGEO4049

Title: Capability of cross-hole electrical configurations for monitoring rapid plume migration experiments

Article Type: Regular

Keywords: cross-hole electrical resistivity tomography, resistivity imaging, dataset optimization.

Corresponding Author: Mr. Fabian Bellmunt,

Corresponding Author's Institution: University of Barcelona. BKC

First Author: Fabian Bellmunt

Order of Authors: Fabian Bellmunt; Alex Marcuello; Ledo Juanjo; Queralt Pilar

Abstract: Cross-hole electrical resistivity tomography is a useful tool in geotechnical, hydrogeological or fluid/gas plume migration studies. It allows to better characterizing deep subsurface structures and monitoring the involved processes. However, due to the large amount of possible four-electrode combinations between boreholes, the choice of the most efficient ones for rapid plume migration experiments (real-time monitoring) becomes a challenge. In this work, we present a numerical simulation to assess the capabilities and constraints of the most common cross-hole configurations for real-time monitoring. Four-electrode configurations, sensitivity, dependence on the body location and amount of data were taken into account. The experimental results showed that a prior knowledge about configurations capability can be used to greatly reduce amount of data stepwise, in order to adjust the acquisition time to the length of the dynamic process to be monitored, maintaining the maximum potential resolution of each configuration.

Research Highlights

We evaluate the cross-hole resistivity configurations for real-time monitoring.

The anomaly detection and symmetry on the sensitivity pattern is analysed.

An easy way to reduce acquisition time and amount of data for monitoring is presented.

This data reduction preserves the configurations capability and resolution.

Capability of cross-hole electrical configurations for monitoring rapid plume migration experiments

F. Bellmunt[1*], A. Marcuello[1], J. Ledo[1] and P. Queralt[1]

[1] Geomodels - Departament de Geodinàmica i Geofísica. Barcelona Knowledge Campus (BKC). Universitat de Barcelona. Martí i Franquès s/n, 08028. Barcelona, Spain.

[*] Corresponding author e-mail: fbellmunt@ub.edu

ABSTRACT

Cross-hole electrical resistivity tomography is a useful tool in geotechnical, hydrogeological or fluid/gas plume migration studies. It allows to better characterizing deep subsurface structures and monitoring the involved processes. However, due to the large amount of possible four-electrode combinations between boreholes, the choice of the most efficient ones for rapid plume migration experiments (real-time monitoring) becomes a challenge. In this work, we present a numerical simulation to assess the capabilities and constraints of the most common cross-hole configurations for real-time monitoring. Four-electrode configurations, sensitivity, dependence on the body location and amount of data were taken into account. The experimental results showed that a prior knowledge about configurations capability can be used to greatly reduce amount of data stepwise, in order to adjust the acquisition time to the length of the dynamic process to be monitored, maintaining the maximum potential resolution of each configuration.

Keywords: cross-hole electrical resistivity tomography, resistivity imaging, dataset optimization.

1. INTRODUCTION

Cross-hole electrical resistivity tomography (CHERT) consists of acquiring electrical resistivity measurements between two or more boreholes and aims imaging the resistivity distribution between them. Since electrodes are down in boreholes, CHERT allows imaging deeper areas and helps to improve resolution at depth.

Monitoring time-lapse evolution of fluids or gas plumes injected in boreholes (Barker and Moore, 1998; Slater et al., 2000; Kiessling et al., 2010; Hagrey and Petersen, 2011; Carrigan et al., 2013) or urban tunnel drillings (Denis et al., 2002; Gibert et al., 2006; Chambers et al., 2007; Bellmunt et al., 2012) using CHERT is becoming common because of the simple and quick data acquisition. However, when rapid migration processes are going to be monitored, the acquisition time becomes critical because it has to be adjusted to the length of the dynamic process. Significant resistivity changes during data acquisition could lead to low resolution images and low convergence of data (Wilkinson et al., 2010). The acquisition time is directly related to the amount of data and the multichannel acquisition efficiency (Bellmunt and Marcuello, 2011). As a general rule, increasing the amount of data will increase resolution, but the improvement begins to level off at large amount of data. The dataset that includes all the standard and non-standard (non-reciprocal) measurements, named comprehensive dataset (Stummer et al., 2004) will contain the maximum resolution. However, the huge amount of data makes it of unrealistic application.

The recent researches in electrical resistivity tomography are focused on searching limited electrode combinations that are comparable in quality to the comprehensive dataset by developing optimization algorithms. In these algorithms, the cumulative sensitivity (Furman et al., 2004; Hennig and Weller, 2005) or the model resolution (Stummer et al., 2004; Wilkinson et al., 2006) improvement is evaluated while groups of combinations of the comprehensive dataset are sequentially added to a small base one. Nyquist et al. (2007) compared the optimized array of Stummer et al. (2004) and the standard dipole-dipole array and they conclude that the first one provides better resolution mainly at depth. But they noticed that the optimized dataset required three times the standard dipole-dipole acquisition time.

Wilkinson et al. (2012) constrained the optimization algorithms to choose what they call near-optimal configurations but well suited for multichannel acquisitions.

At present, the optimization algorithms are not included in the commercial software for resistivity data inversion. Therefore, most researchers still use the traditional CHERT configurations. The extended use of the traditional configurations has allowed researchers to establish their main characteristics (Yang and Ward, 1985; Bing and Greenhalgh, 1997, 2000; Wilkinson et al., 2008). As a general rule in electrical resistivity tomography, the smaller the dipoles length, the larger the influence on data of the immediately surrounding boreholes, and, the larger the dipoles length, the larger the influence on data of the central area of the panel between the involved boreholes. However, larger dipoles are more affected by lateral effects from heterogeneities located outside the panel between the involved boreholes, which can produce shadow effects in the resultant inversion models (Nimmer et al., 2008). Tsourlos et al. (2011) detected this shadow effects on single borehole-to-surface ERT experiments, and conclude that they are the consequence of the high symmetrical sensitivity pattern of the in-hole configurations (all the electrodes in the same borehole). They proposed a modified inversion scheme based on a weighted factor to avoid the shadow or symmetric effects of the in-hole configurations. But, they pointed out the difficulty of defining an objective threshold of asymmetry to use in an automatic way and of removing completely the artefacts from configurations with highly symmetrical sensitivity pattern.

This work proposes an organized way to select the most adequate electrode combinations for rapid CHERT monitoring (acquisition protocol) in order to reduce: 1) the amount of data and acquisition time while maintaining the maximum potential benefit of each configuration and 2) the shadow effects inherent to configurations with highly symmetrical sensitivity pattern. The abilities of the most common CHERT configurations are evaluated and compared using 2D numerical models to reduce uncertain on the acquisition protocol using each configuration or a mixed one.

1. DATA ANALYSIS PROCEDURE

Here, we present the methodology followed to analyse the CHERT configurations ability to plume migration monitoring. Figure 1 can help to better understand the meaning of the next expressions, although it will be explained later. The presented procedure consists of three steps:

The first step consists of calculating the relative resistivity variation produced using each configuration by considering the addition of a resistivity anomaly in a homogeneous half-space. This resistivity variation is related to the anomaly detection capability and it is calculated by the following expression:

$$AD = max\left|\frac{\rho - \rho_{HM}}{\rho_{HM}}\right| \quad (1)$$

where AD: Anomaly Detection value (in absolute value); ρ_{HM}: resistivity value obtained using a homogeneous earth. ρ: resistivity value obtained including a resistivity anomaly in the homogeneous earth. Both resistivity values are calculated using the same electrode combination. Similar expressions to evaluate the anomaly effect can be found in Militzer et al. (1979).

The second step consists of calculating the relative difference between two resistivity values calculated for the same electrode combination but, one considering an anomaly located in the panel between two involved boreholes and the other one, with the anomaly located outside the panel. The difference between the two responses is related to the symmetry on the sensitivity pattern. If no resistivity differences between the two responses are detected, it will imply low capacity to resolve the plume migration direction (highly symmetrical sensitivity pattern), and the interpretation will be uncertain. In this work, this difference is calculated by the expression:

$$IOS = max\left|\frac{2(\rho_{in} - \rho_{off})}{\rho_{in} + \rho_{off}}\right| \quad (2)$$

where IOS: In-panel/Off-panel Sensitivity value (absolute value); $\boldsymbol{\rho_{in}}$: resistivity value obtained using

a resistivity anomaly into the panel between two involved boreholes; $\boldsymbol{\rho_{off}}$: resistivity value obtained using the same resistivity anomaly as before but located outside the panel.

The third step consists of selecting the top rated four-electrode combinations of each configuration using the first and second steps results, which leads to reduce the amount of data and the symmetric artefacts. As a general rule, the criterion used is to choice the electrode combinations with the highest AD and IOS. The acquisition time, desired resolution and signal-to-noise ratio have to be considered to make a proper election.

2. APPLICATION

In order to evaluate the CHERT configurations ability (steps 1 and 2 of the data analysis procedure) we designed a 2D numerical experiment simulating a plume migration process. Following, we describe the plume migration model and the CHERT electrode configurations used.

2.1. Plume migration model

The plume migration model (Figure 1) was designed to get knowledge about the AD, but especially about the IOS of the CHERT configurations. It consists of three in-line boreholes, 10 m apart and 20 m in depth, located in a 100 ohm·m homogeneous half-space. 21 electrodes (1 m-spaced) were placed into each borehole. The plume migration process was simulated using three square bodies of side length twice the electrode distance and centred at three different positions of constant depth: 1, 3 and 5 m from BH2, named stages A, B and C, respectively. Two resistivity contrasts (Rc=$\rho_{plume}/\rho_{half\ space}$), emulating a saline ($Rc$=0.1) and a gas ($Rc$=10) plumes, were considered.

The two panels between the three boreholes in Figure 1 have been grey coloured to differentiate between the cross-hole measurements acquired using the BH1 and BH2 (Panel 1) and the ones acquired using BH2 and BH3 (Panel 2). The AD (step 1) was evaluated comparing panel 1 resistivity responses with and without the imbedded anomalies for each migration model stage and the IOS (step 2) was evaluated comparing the panel 1 and panel 2 resistivity responses for each migration model

stage. In all the cases the comparison is made always using the same electrode combination. Note that using the two panels in step 2, two opposite directions for the plume migration are simulated: inward the panel 1 (measuring between boreholes BH1 and BH2) and outward the panel 2 (measuring between boreholes BH2 and BH3). As commented before, no differences between panel 1 and panel 2 responses can lead to obtain resistivity images of uncertain interpretation.

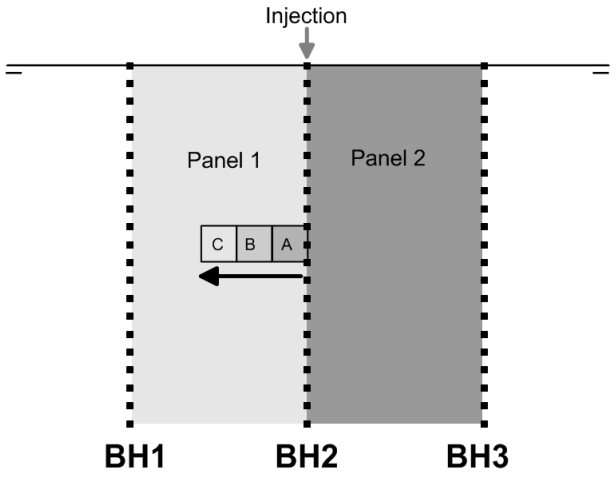

Figure 1. Model and stages used to simulate a plume migration experiment. Small vertical black squares represent the electrode location into boreholes BH1, BH2 and BH3; black arrow and grey squares (named A, B and C) simulate the plume migration at stages A, B and C, respectively. Panel 1 (light grey coloured) represents the cross-hole measurements acquired between BH1 and BH2 and panel 2 (dark grey coloured), the cross-hole measurements acquired between BH2 and BH3.

2.2. CHERT configurations

In this work, we use the term "dipole", instead of “bipole”, to designate the CHERT configurations because of their extensive use in the surface configurations notation, but we add the prefix CH (cross-hole). This experiment is focused on the CH dipole-dipole arrays (CH AM-BN and CH AB-MN), and the CH pole-tripole (CH AMN-B/A-BMN) array (Bing and Greenhalgh, 2000; Goes and Meekes, 2004), which are summarized in Figure 2. Capital letters designate the electrodes (A and B represent the current electrodes and, M and N, the potential ones) and their position into the boreholes (i.e. AM-BN means that the A and M electrodes are located in one borehole and the B and N, in the other one).

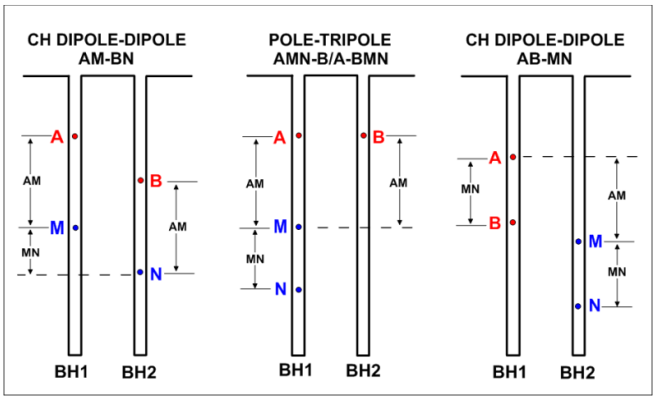

Figure 2. Electrode distribution scheme for the CH dipole-dipole arrays (CH AM-BN and CH AB-MN) and the CH pole-tripole array with the MN dipole in the two boreholes (CH AMN-B/A-BMN). Capital letters and red/blue points designate the electrode name and their position into the boreholes (A and B represent the current electrodes and, M and N, the potential ones); AM: vertical distance between the current and the potential electrodes; MN: vertical distance between the potential electrodes.

The configurations responses to the model (stages A to C) presented in Figure 1 were calculated using the commercial Earthimager 2D software (AGI, Advanced Geosciences, Inc.) with a lateral extended four-element mesh. The CH dipole-dipole AM-BN responses were calculated moving up and down the electrodes but maintaining the distance between the electrodes A and M always equal to the B and N electrodes distance, which resulted in a datasets of 5740 combinations, 2870 per panel using the resistivity model presented in Figure 1. The CH dipole-dipole AB-MN responses were calculated using the current electrodes (A and B) distance always equal to the potential electrodes (M and N) one, obtaining 5740 combinations (2870 per panel). And the CH pole-tripole (AMN-B/A-BMN) responses were calculated moving up and down the electrodes but always maintaining the electrodes A and B at the same depth, which resulted in 3080 combinations (1540 per panel). The AM and MN distances used do not include all the possible four-electrode combinations for each configuration, but they are considered the most representative distances for each configuration.

3. RESULTS

Following, we present the results obtained by applying the proposed methodology to the CH dipole-dipole (AM-BN, AB-MN) and the CH pole-tripole arrays using the migration model presented in

Figure 1 and considering two resistivity contrasts, *Rc*=0.1 and *Rc*=10. The magnitudes of AD and IOS for each configuration were calculated versus different AM and MN distances.

3.1. Resistivity contrast *Rc*=0.1

The results of applying the presented methodology to three plume bodies of resistivity 10 ohm·m in a 100 ohm·m half-space are presented below.

3.1.1. Anomaly detection value, AD

Figure 3 shows the AD results for each configuration versus different AM and MN distances. The maximum AD is obtained for the CH dipole-dipole AB-MN and CH pole-tripole arrays at all the three stages of the migration model.

The AD presents a quite similar behaviour for all the three configurations used (Figure 3). As expected, the higher AD is obtained at stage A (Figure 1), because of the plume is closer to the boreholes. When the plume moves from stage A to stage C, the AD decreases and larger AM distances are needed to detect the plume. Once the maximum value is reached, the AD decreases and tends to level off. This decrease is rapidly accentuated when the AM distance becomes higher than the boreholes distance. However, each configuration presents a slightly different AD pattern (Figure 3).

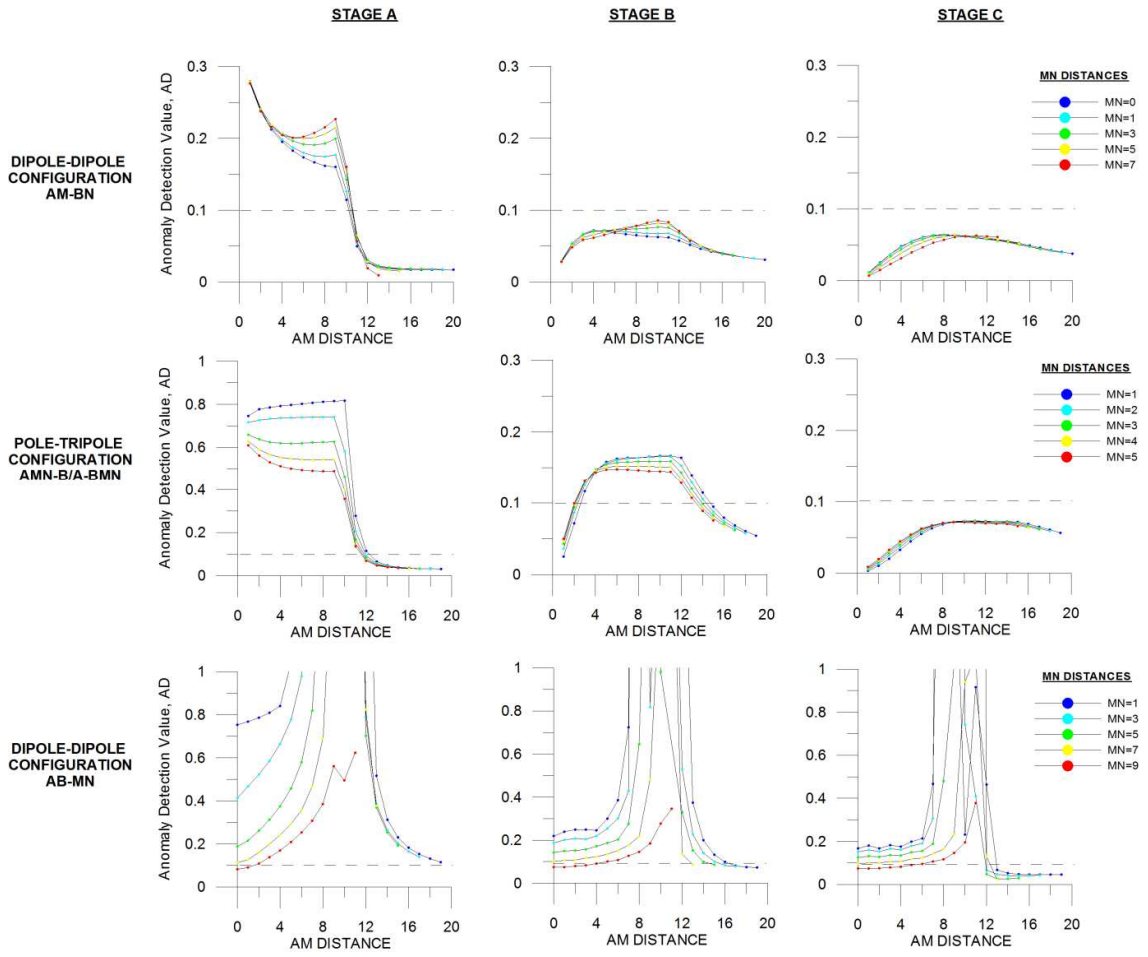

Figure 3. Anomaly detection value, AD, calculated for the CH dipole-dipole (AM-BN and AB-MN) and the CH pole-tripole arrays at the three stages (A, B and C) of the migration experiment using a resistivity contrast *Rc*=0.1. Maximum absolute relative resistivity variation (Y-axis) versus AM (X-axis) and MN (coloured lines) distances. Dashed line indicates a 10% of resistivity change as guidance only.

For the CH AM-BN array, the maximum AD obtained with equation (1) at stages A, B and C were 28%, 8% and 6%, respectively. As the MN distance increases, a secondary AD peak is exhibit when the AM distance becomes similar to the boreholes distance (10 m). This secondary peak becomes higher than the primary one at stage B of the migration model.

For the CH pole-tripole array (AMN-B/A-BMN), the maximum AD obtained at stages A, B and C were 82%, 17% and 7%, respectively. Once the maximum values are reached, this configuration

presents a flat area of maximum AD before starting to decrease. The AD decreases as the MN distance increases.

The CH AB-MN array exhibits extremely high values (higher than 100%) for all the three model stages when the AM value becomes similar to the boreholes distance. For AM distances lower than six, out of the interval of extremely high values, AD is of about 80%, 25% and 20% for stages A, B and C respectively. As the MN distance increases, the AD decreases.

3.1.2. In-panel/off-panel sensitivity value, IOS

Figure 4 shows the IOS results for each configuration versus different AM and MN distances. The maximum IOS using Rc=0.1 is obtained for the CH dipole-dipole AB-MN and the CH pole-tripole arrays at all the stages of the migration model.

The IOS presents a similar behaviour than the AD does: the higher values are obtained at stage A and as the plume moves from stage A to C, the IOS decreases. Once the maximum IOS is reached, it rapidly decreases. However, the maximum IOS is always obtained using AM=10-12 for all the studied configurations and stages of the migration model.

For the CH AM-BN array, the maximum IOS obtained at stages A, B and C were 20%, 8% and 6%, respectively. As the MN values increase, the IOS increases.

For the CH pole-tripole array, the maximum IOS obtained at stages A, B and C were 70%, 10% and 9%, respectively. In this case, as the MN values increase, the IOS decreases.

The CH AB-MN array presents the highest IOS, but extremely high values are detected for AM distances similar to the boreholes distance. As the MN values increase, the IOS decreases.

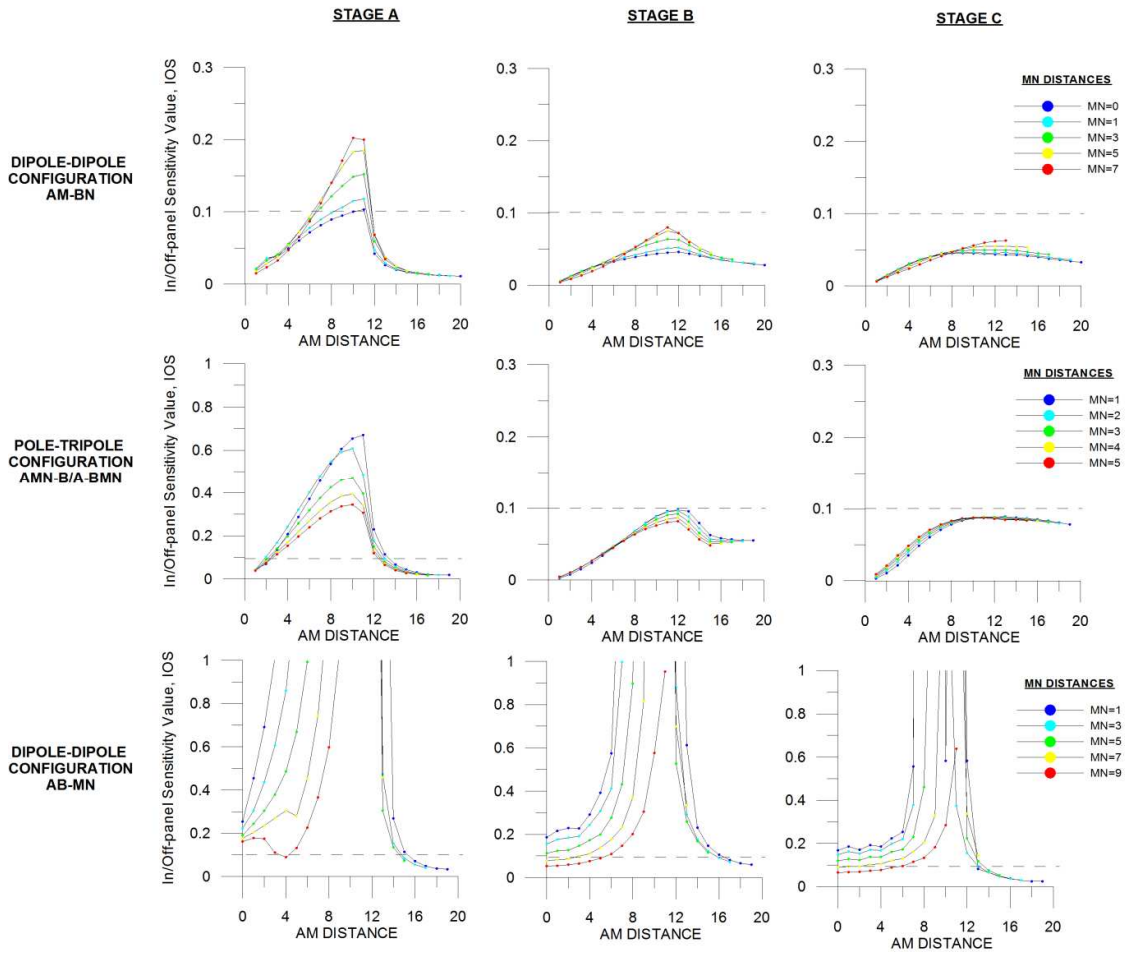

Figure 4. In-panel/off-panel sensitivity value, IOS, calculated using the CH dipole-dipole (AM-BN and AB-MN) and the CH pole-tripole arrays for all the three stages (A, B and C) of the plume migration experiment and a resistivity contrast, *Rc*=0.1. Maximum absolute relative resistivity difference (Y-axis) versus AM (X-axis) and MN (coloured lines) distances. Dashed line indicates a 10% of resistivity difference as guidance only.

3.2. Resistivity contrast *Rc*=10

The procedure application results obtained using plume bodies of 100 ohm·m in a 1000 ohm m half-space, are presented below.

3.2.1. Anomaly detection value, AD

Figure 5 shows the main results obtained for the AD using *Rc*=10. The curves obtained using *Rc*=0.1 and *Rc*=10 (Figure 3 and 5) show that the AD follows a similar behaviour in front different resistivity contrasts, but with slightly different values. In general, the AD obtained using *Rc*=10 is slightly lower

than the one reached using *Rc*=0.1. Therefore, the results obtained using *Rc*=10 will be explained mainly focused on the differences observed from the previous resistivity contrast.

For the CH AM-BN array, the maximum AD obtained at stages A, B and C were 16%, 9% and 8%, respectively. In this case, as the MN distances increase, the secondary AD peak becomes higher than the primary one at all the stages of the migration model.

For the CH pole-tripole array, the maximum AD obtained at stages A, B and C were 82%, 14% and 7%, respectively. In this case, the maximum AD tends to level off, but much slowly than it does using *Rc*=0.1 (compare Figure 3 and 5).

The CH AB-MN array exhibits the same extremely high values as the ones obtained using *Rc*=0.1. However, for small AM distances the AD increases faster than using a conductive anomaly (compare Figure 3 and 5).

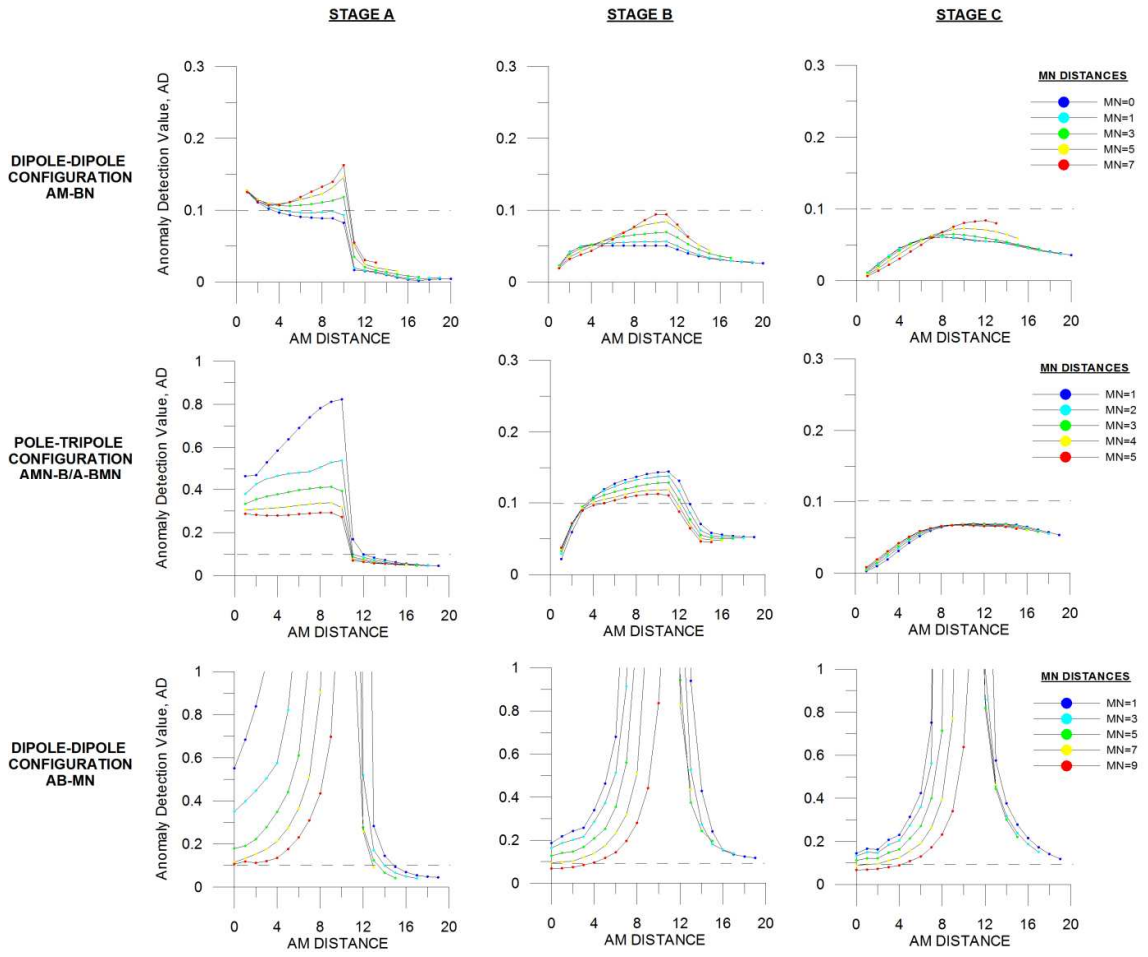

Figure 5. Anomaly detection value, AD, calculated for the CH dipole-dipole (AM-BN and AB-MN) and the CH pole-tripole arrays at the three stages (A, B and C) of the plume migration experiment using a resistivity contrast, *Rc*=10. Maximum absolute relative resistivity variation (Y-axis) versus AM (X-axis) and MN (coloured lines) distances using panel 1. Dashed line indicates a 10% of resistivity change as guidance only.

3.2.2. In-panel/off-panel sensitivity value, IOS

Figure 6 shows the main results for the IOS using *Rc*=10. As the AD does, the IOS follows a similar behaviour for different resistivity contrasts. Therefore, the results obtained using *Rc*=10 will be explained based on the differences observed from the previous resistivity contrast results.

For the CH AM-BN array, the maximum IOS obtained at stages A, B and C were 27%, 11% and 9%, respectively, which are slightly higher than the ones reached using *Rc*=0.1 (compare Figure 3 and Figure 6). As the MN value increases, the maximum IOS increases.

For the CH pole-tripole array, the maximum IOS obtained at stages A, B and C were 56%, 12% and 7%, respectively. In this case, the values obtained using *Rc*=10 are only higher than the ones reached using *Rc*=0.1 at the stage B (compare Figure 4 and Figure 6) of the migration model. As the MN value increases, the IOS decreases.

The CH AB-MN array presents the highest IOS but extremely high values at AM distances similar to the boreholes distance. As the MN value increases, the IOS decreases.

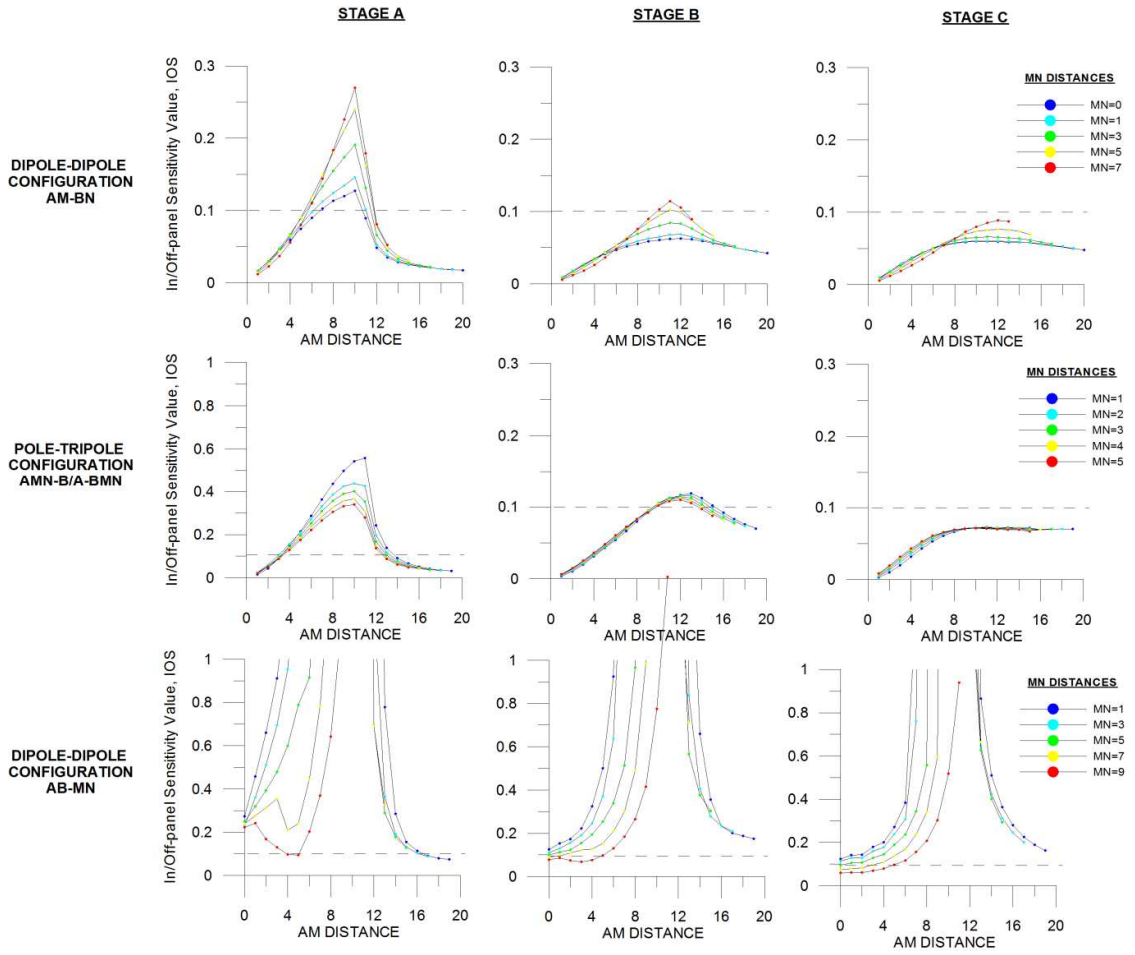

Figure 6. In-panel/off-panel sensitivity value, IOS, calculated using the CH dipole-dipole (AM-BN and AB-MN) and the CH pole-tripole arrays for all the three stages (A, B and C) of the plume migration experiment and a resistivity contrast, *Rc*=10. Maximum relative resistivity variation (Y-axis) versus AM (X-axis) and MN

(coloured lines) distances using panel 1 and panel 2 responses. Dashed line indicates a 10% of resistivity difference as guidance only.

3.3. Organized selection of the combinations

Once the configurations with the best capabilities are detected, the selection of the most suitable combinations can be made in an organized way from the analysis data results. Taking into account the similar AD and IOS behaviour observed using each configuration for different resistivity contrasts (Figures 3 to 6), the organized selection of the combinations is carried out in the same way regardless of the resistivity contrast to be resolved. The analysis results present the CH dipole-dipole AB-MN and the CH pole-tripole arrays as the best choices to migration monitoring using CHERT. In order to reduce amount of data for rapid migration monitoring, where the acquisition time is a critical aspect, the CH dipole-dipole AM-BN array, which shows the lowest AD and IOS, will not be taken into account.

Figures 3 to 6 show that the AD and the IOS patterns are repeated using different MN distances for each configuration. Therefore, the amount of data can be reduced by choosing only one MN distance per configuration. As a general rule, the electrode combinations that correspond to MN values with the highest AD and IOS will offer the maximum potential resolution for monitoring. The number of AM distances has to be chosen in order to cover the central region of the panel (stage C) and to obtain the maximum benefit of the IOS.

Configurations with different (or complementary) sensitivity pattern contributes differently to the model resolution (Bing and Greenhalgh, 1997), therefore a mixed organized dataset can be the best choice. The final organized dataset is made by combining the CH pole-tripole array, taking only the combinations with MN=1 and AM=1-14 (350 combinations per panel), and the CH dipole-dipole AB-MN one with MN=3 and AM=0±5 (168 data per panel). The reason for this choice using the CH dipole-dipole AB-MN array will be treated in the discussion section. The mixed organized dataset results in 518 combinations per panel using model in Figure 1.

4. DATA INVERSION

We carried out the inversion of the mixed organized dataset using the migration model presented in Figure 1 and two resistivity contrasts, *Rc*=0.1 and *Rc*=10. In order to establish the maximum potential model resolution that can be achieved using each of the presented configurations, we made the inversion of the CH pole-tripole dataset with 1540 data per panel and CH dipole-dipole AB-MN one with 1750 data per panel, either individually or in a mixed one (3290 data per panel). The inversion models are presented in Figure 10 (*Rc*=0.1) and Figure 11 (*Rc*=10). Each inversion included panel 1 and panel 2 responses.

The inversion of the datasets was carried out using the commercial Res2dinvx64 software (Geotomo software) with the robust inversion method. To simulate the effect of experimental errors, we added noise using the following expression (Bellmunt and Marcuello, 2011):

$$\Delta R = R\delta + \chi$$

where R is the error-free model response, and δ and χ are random numbers. δ follows a normal distribution with zero mean and standard deviation σ, and χ a uniform distribution in the interval [$-\varepsilon$, $+\varepsilon$]. These two random numbers (δ, χ) simulate the relative accuracy (δ) and the instrumental resolution (χ). A values of 0.015 for σ and 10^{-4} V/A for ε were considered. These values would correspond to a maximum error of 3%, which we consider acceptable for CHERT acquisitions.

As can be seen in Figure 10 (*Rc*=0.1), the CH dipole-dipole AB-MN and the CH pole-tripole inversion models are not able to fully resolve the migration experiment presented here. Although the plume body is located inside the panel 1, the CH pole-tripole inversion model shows an artefact on panel 2 in a "symmetric" location (Nimmer et al., 2008; Tsourlos et al., 2011). The CH dipole-dipole AB-MN inversion model presents much more artefacts than the CH pole-tripole one, but they are mainly distributed along boreholes. The inversion model obtained joining them in a mixed dataset, reaches the

maximum resolution and it is able to recover all the model stages of the migration model. Figure 10 shows that the inversion models obtained using the mixed organized dataset are able to track the plume as well as the complete mixed one.

The inversion models obtained using a resistivity contrast, Rc=10, show less artefacts than the obtained using Rc=0.1, but the plume resistivity value is worst recovered (Figure 11). In this case, individual and mixed inversions using the CH pole-tripole and the CH dipole-dipole AB-MN datasets are able to resolve the migration model, but the maximum resolution is achieved, as before, using the mixed one. The mixed organized dataset is able to resolve all the stages of the migration model, but the anomaly resistivity value at stage C is worst recovered than using the complete mixed one.

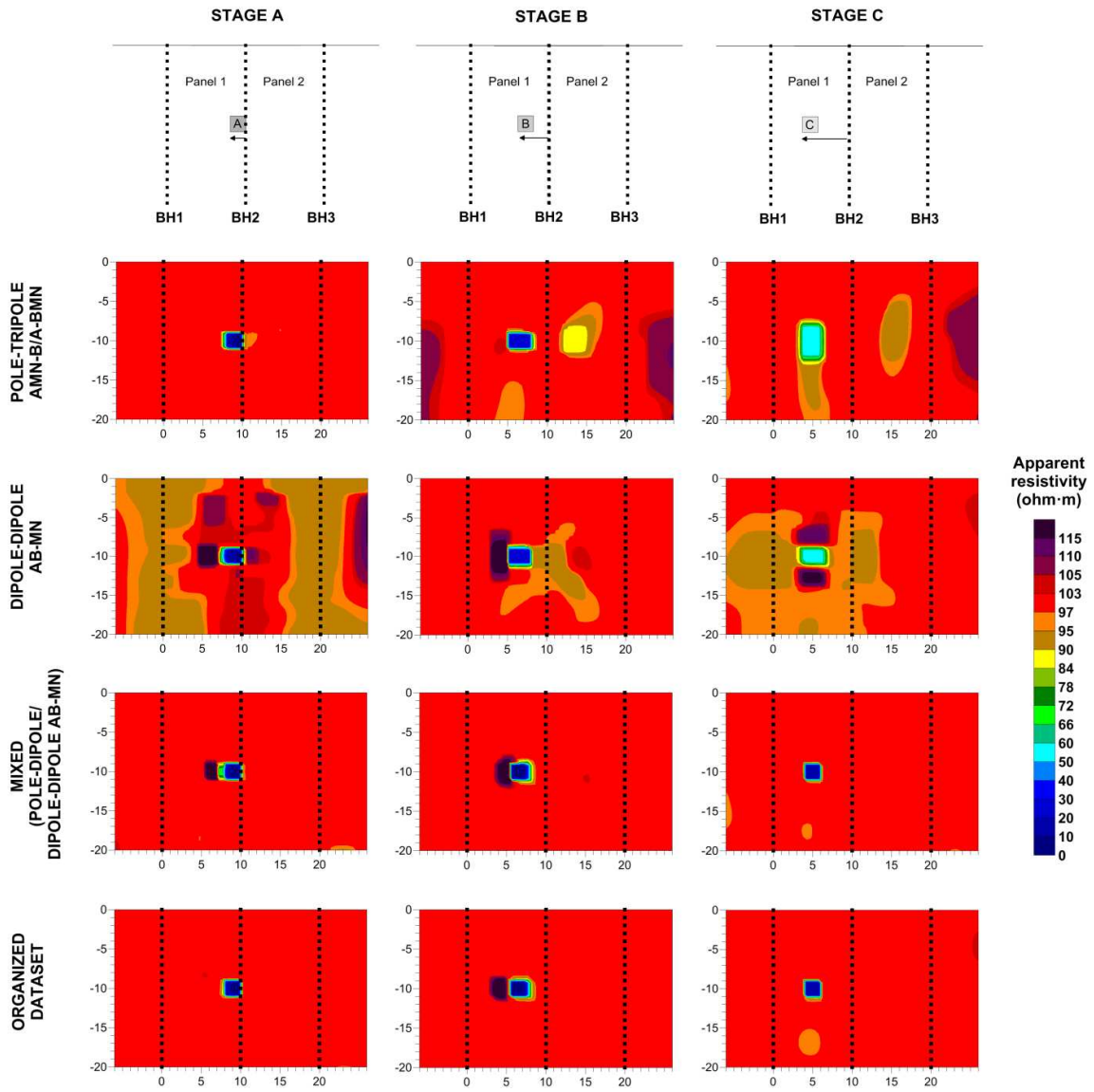

Figure 7. Inversion models obtained using (from top to bottom) the CH pole-tripole (3080 data), the CH dipole-dipole AB-MN (3500 data), the complete mixed (CH pole-tripole and CH dipole-dipole AB-MN with 6580 data) and the mixed organized (1036 data) datasets at the three stages (A, B and C) of the migration model. Resistivity contrast *Rc*=0.1. Root mean square (rms) =1.2%. Small vertical black squares represent the electrode location into boreholes (BH1, BH2 and BH3). Each inversion included panel 1 and panel 2 responses.

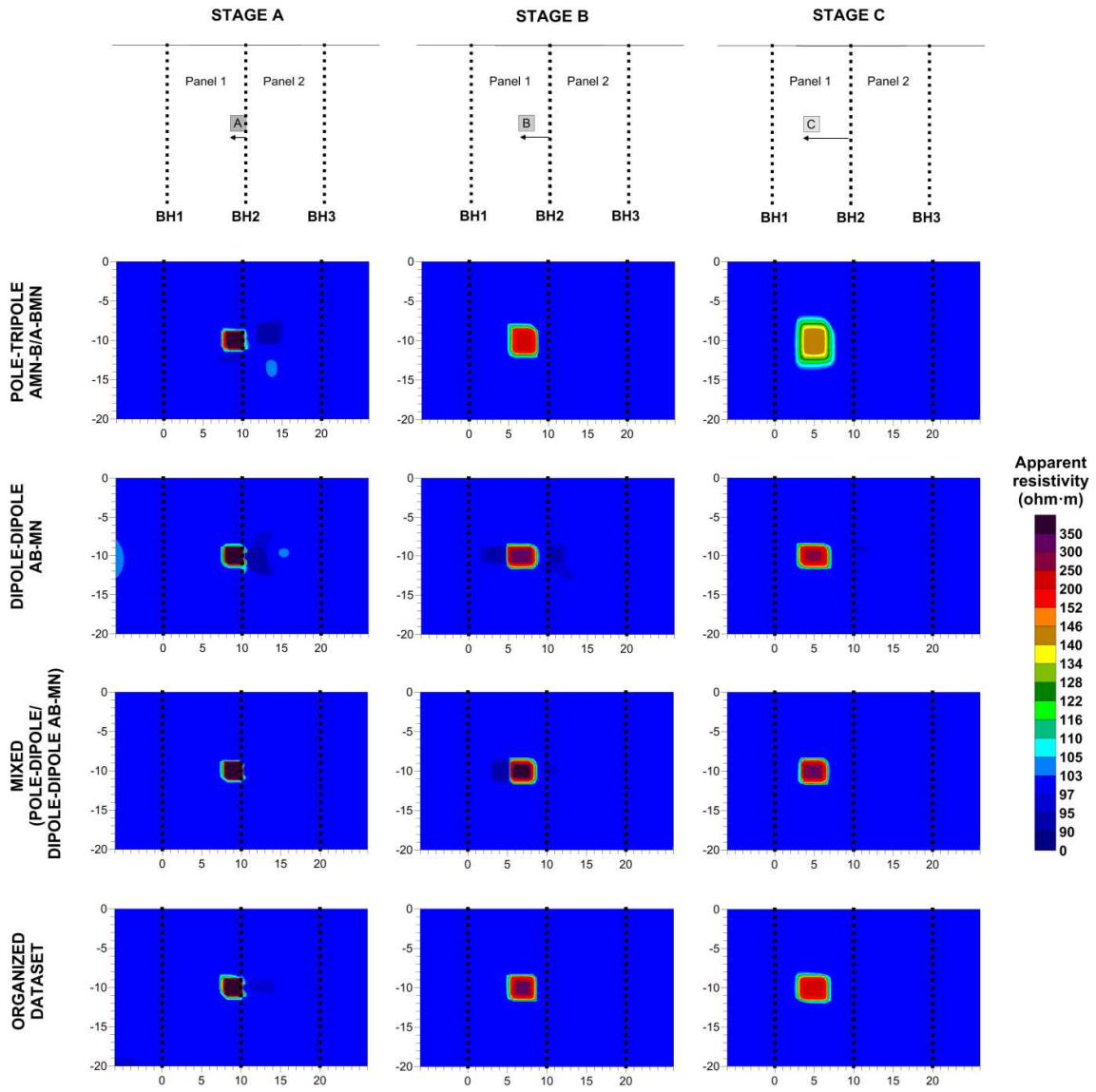

Figure 8. Inversion models obtained using (from top to bottom) the CH pole-tripole (3080 data), the CH dipole-dipole AB-MN (3500 data), the complete mixed (CH pole-tripole and CH dipole-dipole AB-MN with 6580 data) and the mixed organized (1036 data) datasets at the three stages (A, B and C) of the migration experiment using a resistivity contrast *Rc*=10. Root mean square (rms)=1.2%. Small vertical black squares represent the electrode location into boreholes (BH1 and BH2). Each inversion included panel 1 and panel 2 responses.

5. DISCUSSION

In this section we will discuss firstly the behaviour observed for the AD using the CH dipole-dipole arrays and secondly the symmetric artefacts that affects the inversion models using *Rc*=0.1.

The AD graphs in Figures 3 and 5 show that the CH dipole-dipole AM-BN array exhibits a secondary AD peak and the CH dipole-dipole AB-MN array shows extremely high AD for all the three model stages. These maximums could be related to the electric potential drop while changing the AM and MN distances (Wilkinson et al., 2008). Usually, the geometric factor is used as a representative of the inverse of the electric potential for a homogeneous half-space (using a 1 ohm·m resistivity and an intensity of 1 A) and high geometric factor values represent low potential readings and inversely. The Figure 9 shows the general behaviour of the geometric factor for the CH dipole-dipole arrays: AM-BN and AB-MN. Note the AM distance can be positive or negative using the CH dipole-dipole AB-MN array (Figure 3). As can be seen in Figure 9A, as the MN distance increases, the geometric factor value for the CH dipole-dipole AM-BN array becomes more upright at lower AM distances, and finally there is a sign change. This means that there is a sharply drop in the electric potential at those AM and MN distances. This explains why, as the MN distance increases, the secondary AD peak becomes higher. In this situation, low variations in the model response calculation can be in a high resistivity variation. The Figure 9B shows that the CH dipole-dipole AB-MN geometric factor values rise highly when the AM distance increases. As before, this is related with a sharply drop in the electric potential, but in this case, the lower the MN distances, the higher the geometric factor values (or the lower the potential difference). In order to maintain a trade-off between the AD and the electric potential value using any of these two configurations, the AM-BN combinations with MN>7 and AM>10 and the AB-MN combinations with MN=1-2 and AM>±5 should be avoided.

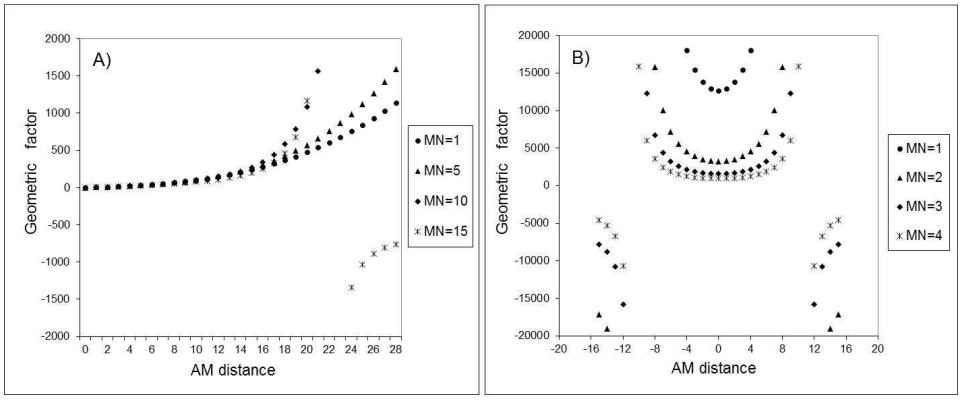

Figure 9. Geometric factor behaviour obtained using the CH dipole-dipole arrays. A) CH AM-BN and B) CH AB-MN with different AM and MN distances.

The CH pole-tripole inversion models at the stages B and C of the migration experiment show "symmetric" artefacts using *Rc*=0.1 (Figure 7). The CH dipole-dipole AM-BN inversion models (not shown here) exhibit the same artefact at the same stages. This symmetric artefact is related to the high symmetry on the sensitivity pattern (Tsourlos et al., 2011) along with to an insufficient angular coverage. The CH pole-tripole and the CH AM-BN arrays show IOS<10%, which means they have highly symmetric sensitivity patterns. The higher the symmetry on the sensitivity pattern, the higher the uncertain on the migration interpretation, and higher angular coverage is needed to resolve the true anomaly location. Increasing amount of data by adding extra angular measurements (combinations with different AM distances), makes the value of the artefact slightly decreases, but they do not removes it at all, either using individual or mixed datasets.

4. CONCLUSIONS

The analysis of the AD and IOS allow finding a trade-off between the required resolution and the available acquisition time (amount of data) for real-time monitoring. Understanding how each configuration works becomes a key aspect to be successful in monitoring short and quick dynamical processes, where the amount of data needs to be greatly reduced to adequate to the experiment length. The AD and IOS analysis has been applied to a specific migration model (using specific body lengths, resistivity contrasts and aspect ratio between boreholes distance and depth) and configurations, but it can be applied to other resistivity models and electrode combinations in a straightforward way.

The results highlight the benefit of joining various configurations because of their different sensitivity pattern: a lower angular coverage and a lower amount of data are needed to resolve a migration experiment. High symmetric sensitivity pattern is a limiting aspect to migration monitoring. Therefore, and considering that most of the CHERT configurations have a quite similar sensitivity pattern, the CH dipole-dipole AB-MN becomes necessary to resolve the migration model presented here and to remove the symmetric artefact. As can be seen in this work, the singularity acquisition problems can be avoided to use this configuration in monitoring.

The similar IOS patterns observed for all the three configurations highlights the need for using AM lengths similar to the boreholes distance in cross-hole monitoring experiments.

The addition of more than one MN distance in the same dataset will help to improve resolution. However, before increasing amount of data by adding various MN distances, consider joining configurations with complementary sensitivity patterns. This provides better spatial resolution without greatly increasing the amount of data. In this work, a mixed organized dataset, which can be acquired in less than 10 minutes (1036 data) in a ten-simultaneous channels resistivity-meter, has been able to resolve the migration model presented here without the presence of symmetric artefacts. This allows acquiring multi-panel or 3D data in a time-effective way.

ACKNOWLEDGEMENTS

This work was partially supported by the Spanish Ministry of Economy and Competitiveness and EU FEDER funds under projects Geothercan (IPT-2011-1186-920000) and COMOSALTS (CGL2014-54118-C02-01-R) and by the Catalan Agency AGAUR through the Group "Geodynamics and Basin Analysis" (2014SGR467).

REFERENCES

Barker, R., Moore, J., 1998. The application of time-lapse electrical tomography in groundwater studies. Lead. Edge 17, p. 1454-1458.

Bellmunt, F. and Marcuello, A., 2011. Method to obtain standard pseudosections from pseudo pole–dipole arrays. Journal of Applied Geophysics 75, p. 419–430.

Bellmunt, F., Marcuello, A., Ledo, J., Queralt, P., Falgàs, E., Benjumea, B., Velasco, V., Vázquez-Suñé, E., 2012. Time-lapse cross-hole electrical resistivity tomography monitoring effects of an urban tunnel. Journal of Applied Geophysics, 87, p. 60–70.

Bing, Z., Greenhalgh, S.A., 1997. A synthetic study on cross-hole resistivity imaging with different electrode arrays. Explor. Geophys. 28, p. 1-5.

Bing, Z., Greenhalgh, S.A., 2000. Cross-hole resistivity tomography using different electrode configurations. Geophysical Prospecting 48, p. 887–912.

Carrigan, C.R., Yang, X., LaBrecque, D.J., Larsen, D., Freeman, D., Ramírez, A.L., Daily, W., Newmark, R., Friedman, J., Hovorka, S., 2013. Electrical resistance tomographic monitoring of CO2 movement in deep geologic reservoirs. International Journal of Greenhouse Gas Control. 8, p. 401-408.

Chambers, J.E., Wilkinson, P.B., Weller, A.L., Meldrum, P.I., Ogilvy, R.D., Caunt, S., 2007. Mineshaft imaging using surface and crosshole 3D electrical resistivity tomography: A case history from the East Pennine Coalfield, UK. Journal of Applied Geophys. 62, p. 324-337.

Denis, A., Marache, A., Obellianne, T., Breysse, D., 2002. Electrical resistivity borehole measurements: an application to an urban tunnel site. J. Appl. Geophys. 50, p. 319-331.

Furman, A., Ferré, T.P.A., Warrick. A.W., 2004. Optimization of ERT surveys for monitoring transient hydrological events using perturbation sensitivity and genetic algorithms. Vadose Zone Journal 3, p. 1230-1239.

Gibert, D., Nicollin, F., Kergosien, B., Bossart, P., Nussbaum, C., Grislin-Mouëzy, A., Conil, F., Hoteit, N., 2006. Electrical tomography monitoring of the excavation damaged zone of the Gallery 04 in the Mont Terri rock laboratory: Field experiments, modelling, and relationship with structural geology. Appl. Clay Sci. 33, 21-34.

Goes, B.J.M. and Meekes, J.A.C., 2004. An effective electrode configuration for the detection of DNAPLs with electrical resistivity tomography. Journal of Environmental and Engineering Geophysics, 9, p. 127-141.

Hagrey, S.A. and Petersen, T., 2011. Numerical and experimental mapping of small root zones using optimized surface and borehole resistivity tomography. Geophysics, vol. 76, n 2, p. G25-G35.

Hennig, T. and Weller, A., 2005. Two dimensional object orientated focussing of geoelectrical multielectrode measurements. Proceedings of the 11th meeting of the EAGE Near Surface Geophysics Conference, Palermo, Italy.

Kiessling, D., Schmidt-Hattenberger, C., Schuett, H., Schilling, F., Krueger, K., Schoebel, B., Danckwardt, E., Kummerow, J., and the CO2sink Group, 2010. Geoelectrical methods for monitoring geological CO2 storage: First results from cross-hole and surface-downhole measurements from the CO2SINK test site at Ketzin (Germany). International Journal of Greenhouse Gas Control, 4, p. 816-826.

Militzer, H., Rösler, R. and Lösch, W., 1979. Theoretical and experimental investigations for cavity research with geoelectrical resistivity methods. Geophysical Prospecting, 27, p. 640–652.

Nimmer, R.E., Osiensky, J.L., Binley, A.M., Williams, B.C., 2008. Three-dimensional effects causing artifacts in twodimensional, cross-borehole, electrical imaging. Journal of Hydrology, 359, p. 59-70.

Nyquist, J. E., Peake, J. S., Roth M. J. S., 2007. Comparison of an optimized resistivity array with dipole-dipole soundings in karst terrain. Comparison of an optimized resistivity array with dipole-dipole soundings in karst terrain, 72(4), F139-F144.

Slater, L., Binley, A.M., Daily, W. and Johnson, R., 2000. Cross-hole electrical imaging of a controlled saline tracer Injection. Journal of Applied Geophysics 44, p. 85–102.

Stummer, P., Maurer, H., and Green, A.G., 2004. Experimental design: electrical resistivity data sets that provide optimum subsurface information. Geophysics, 69, n 1, pp.120–139.

Tsourlos, P., Ogilvy, R., Papazachos, C., Meldrum, P., 2011. Measurement and inversion schemes for single borehole-to-surface electrical resistivity tomography surveys. Journal of Geophysics and Engineering, vol. 8, n 4.

Wilkinson, P. B., Meldrum, P. I., Chambers, J. E., Kuras, O., and Ogilvy, R. D., 2006. Improved strategies for the automatic selection of optimised sets of electrical resistivity tomography measurement configurations. Geophysical Journal International, 167, p. 1119–1126.

Wilkinson, P. B., Chambers, J.E., Lelliott, M., Wealthall, G.P. and Ogilvy, R.D., 2008. Extreme sensitivity of crosshole electrical resistivity tomography measurements to geometric errors. Geophysical Journal International, 173(1), p. 49-62.

Wilkinson, P.B., Meldrum, P.I., Kuras, O., Chambers, J.E., Holyoake, S.J., Ogilvy, R.D., 2010. High-resolution Electrical Resistivity Tomography monitoring of a tracer test in a confined aquifer. Journal of Applied Geophysics 70, p. 268–276.

Wilkinson, P. B., Loke, M. H., Meldrum, P. I., Chambers, J. E., Kuras, O., Gunn, D. A. and Ogilvy, R.D., 2012. Practical aspects of applied optimized survey design for electrical resistivity tomography. Geophysical Journal International, 189, p. 428–440.

Yang F.W. and Ward S.H., 1985. Single-borehole and cross-borehole resistivity anomalies of thin ellipsoids and spheroids. Geophysics, vol. 50, n. 4, p. 637-655.

FIGURE CAPTIONS

Figure 1. Model and stages used to simulate a plume migration experiment. Small vertical black squares represent the electrode location into boreholes BH1, BH2 and BH3; black arrow and grey squares (named A, B and C) simulate the plume migration at stages A, B and C, respectively. Panel 1 (light grey coloured) represents the cross-hole measurements acquired between BH1 and BH2 and panel 2 (dark grey coloured), the cross-hole measurements acquired between BH2 and BH3.

Figure 2. Electrode distribution scheme for the CH dipole-dipole arrays (CH AM-BN and CH AB-MN) and the CH pole-tripole array with the MN dipole in the two boreholes (CH AMN-B/A-BMN). Capital letters and red/blue points designate the electrode name and their position into the boreholes (A and B represent the current electrodes and, M and N, the potential ones); AM: vertical distance between the current and the potential electrodes; MN: vertical distance between the potential electrodes.

Figure 3. Anomaly detection value, AD, calculated for the CH dipole-dipole (AM-BN and AB-MN) and the CH pole-tripole arrays at the three stages (A, B and C) of the migration experiment using a resistivity contrast *Rc*=0.1. Maximum absolute relative resistivity variation (Y-axis) versus AM (X-axis) and MN (coloured lines) distances. Dashed line indicates a 10% of resistivity change as guidance only.

Figure 4. In-panel/off-panel sensitivity value, IOS, calculated using the CH dipole-dipole (AM-BN and AB-MN) and the CH pole-tripole arrays for all the three stages (A, B and C) of the plume migration experiment and a resistivity contrast, *Rc*=0.1. Maximum absolute relative resistivity difference (Y-axis) versus AM (X-axis) and MN (coloured lines) distances. Dashed line indicates a 10% of resistivity difference as guidance only.

Figure 5. Anomaly detection value, AD, calculated for the CH dipole-dipole (AM-BN and AB-MN) and the CH pole-tripole arrays at the three stages (A, B and C) of the plume migration experiment using a resistivity contrast, *Rc*=10. Maximum absolute relative resistivity variation (Y-axis) versus AM (X-axis) and MN (coloured lines) distances using panel 1. Dashed line indicates a 10% of resistivity change as guidance only.

Figure 6. In-panel/off-panel sensitivity value, IOS, calculated using the CH dipole-dipole (AM-BN and AB-MN) and the CH pole-tripole arrays for all the three stages (A, B and C) of the plume migration experiment and a resistivity contrast, *Rc*=10. Maximum relative resistivity variation (Y-axis) versus AM (X-axis) and MN (coloured lines) distances using panel 1 and panel 2 responses. Dashed line indicates a 10% of resistivity difference as guidance only.

Figure 7. Inversion models obtained using (from top to bottom) the CH pole-tripole (3080 data), the CH dipole-dipole AB-MN (3500 data), the complete mixed (CH pole-tripole and CH dipole-dipole AB-MN with 6580 data) and the mixed organized (1036 data) datasets at the three stages (A, B and C) of the migration model. Resistivity contrast *Rc*=0.1. Root mean square (rms) =1.2%. Small vertical black squares represent the electrode location into boreholes (BH1, BH2 and BH3). Each inversion included panel 1 and panel 2 responses.

Figure 8. Inversion models obtained using (from top to bottom) the CH pole-tripole (3080 data), the CH dipole-dipole AB-MN (3500 data), the complete mixed (CH pole-tripole and CH dipole-dipole AB-MN with 6580 data) and the mixed organized (1036 data) datasets at the three stages (A, B and C) of the migration experiment using a resistivity contrast *Rc*=10. Root mean square (rms)=1.2%. Small vertical black squares represent the electrode location into boreholes (BH1 and BH2). Each inversion included panel 1 and panel 2 responses.

Figure 9. Geometric factor behaviour obtained using the CH dipole-dipole arrays. A) CH AM-BN and B) CH AB-MN with different AM and MN distances.